Validation of the resistance of a plate moving through mud
CFD modelling and towing tank experiments

Lovato, S.; Kirichek, Alex ; Toxopeus, S.L.; Settels, J.W.; Keetels, G.H.

DOI
10.1016/j.oceaneng.2022.111632

Publication date
2022

Document Version
Final published version

Published in
Ocean Engineering

Ocean Engineering 258 (2022) 111632

Contents lists available at ScienceDirect

Ocean Engineering

journal homepage: www.elsevier.com/locate/oceaneng

Validation of the resistance of a plate moving through mud: CFD modelling and towing tank experiments

S. Lovato [a,*], A. Kirichek [b], S.L. Toxopeus [c], J.W. Settels [c], G.H. Keetels [a]

[a] Section of Offshore and Dredging Engineering, Department of Maritime and Transport Engineering, Faculty of Mechanical, Maritime and Materials Engineering, Delft University of Technology, Leeghwaterstraat 2, 2628 CA Delft, The Netherlands

[b] Section of Rivers, Ports, Waterways and Dredging Engineering, Department of Hydraulic Engineering, Faculty of Civil Engineering & Geosciences, Delft University of Technology, Stevinweg 1, 2628 CN Delft, The Netherlands

[c] Maritime Research Institute Netherlands, P.O. Box 28, Wageningen 6700AA, The Netherlands

ARTICLE INFO

Keywords:
Mud
Bingham
Yield stress
CFD
Plate
Non-Newtonian
Friction

ABSTRACT

When investigating the effect of muddy seabeds on marine vessels using Computational Fluid Dynamics (CFD) software, one challenge is to adequately describe the complex non-Newtonian fluid behaviour of mud. Although a number of rheological models have been proposed in the past, mud sediments are often simply regarded either as highly viscous Newtonian fluids or as Bingham fluids in many engineering applications. In this study, we investigate the accuracy of the Bingham model for numerical predictions of the viscous forces on a plate moving through fluid mud in laminar regime. In this context, a plate could be regarded as the flat bottom of a ship hull. The aim is to provide CFD practitioners with information about the accuracy of the Bingham model for the prediction of the frictional resistance of a ship sailing through fluid mud. This work presents a comparison of experimental and numerical data on the resistance of a plate moving through fluid mud from the Europoort area (Netherlands). Results suggest that the regularised Bingham model can be a reasonable compromise between simplicity and accuracy for CFD simulations to investigate the effect of muddy seabeds on marine vessels. A comparison between CFD data and analytical formulas is also presented.

1. Introduction

The influence of muddy seabeds on the ships' manoeuvring behaviour has been studied experimentally, both at full (Barth et al., 2016) and model scales (Sellmeijer and van Oortmerssen, 1984; Delefortrie et al., 2005), for safe navigation in confined waters. However, the outcome of these studies is difficult to generalise because of the large number of parameters involved (under-keel clearance, mud layer thickness, mud properties, ship's geometry and speed, fairway cross-section, etc.) and the complex non-Newtonian behaviour of mud. These reasons, combined with the rapid growth of computing power over the past decades, have made Computational Fluid Dynamics (CFD) the tool of choice.

One of the open questions for CFD simulations of mud flows is selecting a constitutive equation that adequately describes the complex non-Newtonian behaviour of mud. In particular, mud exhibits viscoplasticity and thixotropy. Viscoplastic fluids start to flow only when the shear stress level exceeds a threshold called the yield stress. Below the yield stress, viscoplastic fluids behave as solid-like materials. On the other hand, thixotropy implies that, under constant and sufficiently high shear, the yields stress and viscosity of mud decrease due to changes in the internal microstructure, meaning that the rheological properties are dependent upon the shear history. Depending on the level of approximation required, the complexity of the models can range from the simple Newtonian constitutive equation to the Bingham and Herschel–Bulkley models and ultimately to time-dependent (thixotropic) yield-stress models (see e.g. Chhabra and Richardson (2008) for an overview of non-Newtonian constitutive equations).

More complex models are typically found in rheological studies as their objective is to reproduce the rheology of mud as precisely as possible. Coussot and Piau (1994) showed that mud suspensions can be well described by the Herschel–Bulkley model, which has also been used to characterise the mud from the Port of Emden (Germany) (Wurpts, 2005) and it is recommended by PIANC (McBride et al., 2014). Wright and Krone (1989) used a more complex model that is parametrised with the solid content. Continuing with higher level of complexity, Toorman (1997) proposed a five-parameter thixotropic model that is an extension of the Moore (1959) and Worrall–Tuliani (Worrall and Tuliani, 1964) models. van Kessel and Blom (1998) used

* Corresponding author.
E-mail address: s.l.lovato@tudelft.nl (S. Lovato).

https://doi.org/10.1016/j.oceaneng.2022.111632
Received 24 January 2022; Received in revised form 7 April 2022; Accepted 25 May 2022
Available online 22 June 2022

the Toorman model for a comparison of the rheological properties of artificial and natural mud from the Port of Rotterdam (Netherlands). Recently, Shakeel et al. (2021) proposed a two-step yielding model containing six fitting parameters that was based on the rheological analysis of mud from the Port of Hamburg (Germany) (Shakeel et al., 2020a,b).

Such complex rheological models may be unnecessary for large-scale processes, where in fact simpler models have found their own field of applicability. For example, the wave-induced motions of muddy beds have been studied assimilating the mud to a Bingham fluid (Mei and Liu, 1987; Liu and Mei, 1989; Ko-Fei and Mei, 1993; Chan and Liu, 2009) or a Newtonian fluid (Jiang and Mehta, 1992; Winterwerp et al., 2007). As a counterexample, however, Knoch and Malcherek (2011) used a modified version of the Worrall–Tuliani model for numerical simulations of stratified mud flows in coastal and estuarine environments.

Simple rheological models seem preferred also to study the effect of muddy seabeds on marine vessels, which is the application that motivated this work. The ship-induced undulation at the water–mud interface can result in a very large increase in the resistance due to the internal wave at the water–mud interface. This is also known as the 'dead-water' effect (e.g. Miloh et al. (1993)), which has been studied extensively either using the Newtonian model (Miloh et al., 1993; Zilman and Miloh, 1995) or even assuming inviscid mud (Sano and Kunitake, 2018). These strong simplifications could be justified by the fact that viscosity plays a minor role in gravity waves. Recently, Gao et al. (2015) and Kaidi et al. (2020) have performed CFD simulations to study the influence of muddy seabeds on ships. The former modelled the mud as an Herschel–Bulkley fluid, whereas the latter used the Newtonian model as they observed little difference in the computed resistance when the Bingham model was used.

In summary, simple models are often used for applications where viscosity plays a minor role (e.g. propagation of gravity waves) or where the fluid is highly sheared (e.g. in the boundary layer at the hull of a ship). In fact, CFD practitioners are usually not interested in the quality of the fit to the flow curves but rather in the accuracy of the flow and force predictions. In the present work, the Bingham model is used to characterise the rheology of mud as it is very simple and yet it can capture an important feature of mud, i.e. viscoplasticity. To the best of our knowledge, numerical predictions of the drag forces exerted on bodies moving through mud have not been compared with experiments before. This is an important aspect that can help CFD practitioners in deciding whether a more complex model is required or not.

This work makes a first step forward by investigating the accuracy of the Bingham model for numerical prediction of the resistance of a plate moving through mud in laminar regime. In the context of ships sailing through mud, the plate can be regarded as a part of the flat bottom of a typical ship hull.

The article presents an analysis and comparison of experimental and numerical data. The experiments consist of towing a plate in a towing tank filled with mud from the Europoort area (Rotterdam, Netherlands) and diluted with sea water from the same location. Three mud conditions are considered, all with density below or equal to $1200\,\mathrm{kg/m^3}$, in line with the nautical bottom criterion applied in several harbours across the world (McBride et al., 2014; Kirichek et al., 2018). Numerical simulations were performed using a finite-volume CFD code. Finally, CFD results have been compared with predictions from simple analytical formulas.

2. Experimental data

2.1. Facility and setup

The experimental data were obtained in the 'Water and Soil Flume' at Deltares (Netherlands) (wsf). In the remainder, the flume will be referred to as 'towing tank' as the latter better describes how it was used in this work.

Table 1
Main information about the experiments.

Plate		Towing tank	
Chord, L (m)	0.8	Length (m)	30.0
Thickness, t (m)	0.012	Width (m)	2.4
Draught, T (m)	0.96, 1.0	Mud level, h (m)	1.96, 2.0
Speed, V (m/s)	0.27, 0.52, 0.77, 1.02		
$F_n = V/\sqrt{gL}$	0.10, 0.19, 0.27, 0.36		
$F_{nh} = V/\sqrt{gh}$	0.06, 0.12, 0.17, 0.23		

The towing tank is 30 m long and 2.4 m wide. The experiments consisted in towing a smooth plywood plate through the mud in the tank. The plate was attached to a carriage through a load cell (Fig. 1), which enabled force measurements in the towing direction. The nominal towing speed of the carriage was varied between 0.25 and 1.0 m/s and, for each speed, the tests were repeated eight times in order to estimate the random scatter of the mean force.

The plywood plate has a chord of 0.8 m and it is 0.012 m thick. For the tests with the most dense mud (Mud_23 in Table 2) the plate was submerged by 0.96 m, whereas for all other cases it was 1.0 m. The plate has been reinforced with vertical and horizontal wooden beams to increase its stiffness and to reduce possible bending. The main information about the experimental setup is summarised in Table 1.

To make an analogy with a ship, the aforementioned dimensions correspond to $h/T = 2$, where h and T are the mud depth and the ship's draught, respectively. This depth-to-draught ratio is considered to be shallow enough to influence the forces acting on a sailing ship. However, the relative width of the plate is an order of magnitude lower than expected for a ship, which practically eliminates the blockage and the subsequent shallow water effects.

2.2. Mud preparation

The mud was collected from the Calandkanaal (Europoort, Netherlands) and transported to the towing tank. In order to test the accuracy of the Bingham model on different mud conditions, the mud was diluted with sea water (having the same salinity as the natural system) to obtain three densities that correspond to target yield stress values of approximately 10, 20 and 30 Pa.

To ensure the homogeneous properties within the towing tank, the mud was stirred using a rotating mixer (Fig. 2), which has been towed three times back-and-forth prior the start of the experiments with each mud. After the homogenisation, samples of mud were collected twice (before the start of the experiments and after about six hours) at three specific locations along the towing tank. Thus, six samples for each mud were analysed for the density and the rheological properties.

2.3. Mud density and rheology

The bulk densities of the mud samples were determined by a portable density meter (Anton Paar, DMA 35). The mud rheology was analysed using the HAAKE MARS I rheometer with a concentric cylinder geometry (CC25) having a gap width of 1 mm. A Peltier controller system was utilised to maintain the temperature at 20 °C during each experiment, which was the average temperature in the towing tank.

The flow curves of the mud samples were obtained in controlled shear rate mode with the following protocol: (i) shear rate ramp-up from 0 to $300\,\mathrm{s^{-1}}$ in 180 s, (ii) constant shear rate of $300\,\mathrm{s^{-1}}$ for 60 s, and (iii) shear rate ramp-down from 300 to $0\,\mathrm{s^{-1}}$ in 180 s. This protocol is proven to be quite fast and repeatable to obtain the yield stress of

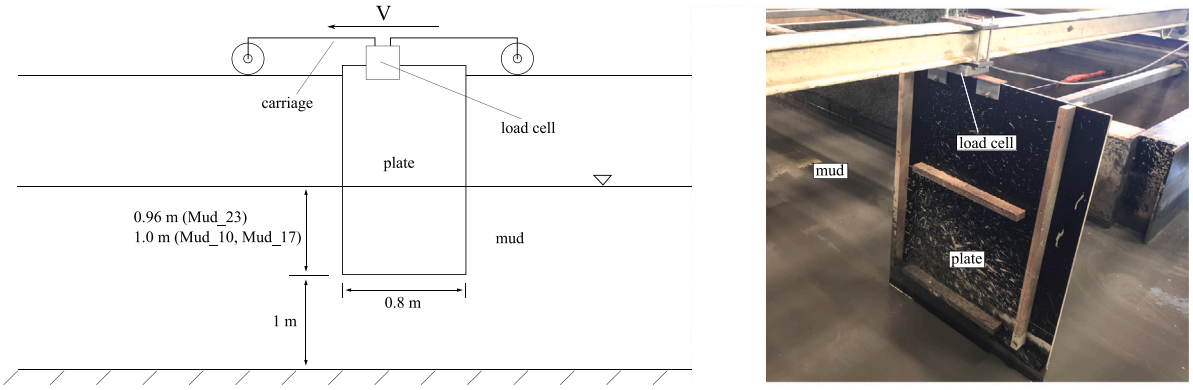

Fig. 1. Schematic representation of the experiments (left) and picture of the plate immersed in mud (right).

Fig. 2. The rotating mixer used to homogenise the mud. The right panel shows the mixer in action.

Table 2
Mean values (± standard uncertainty) of density and Bingham parameters for the three mud dilutions. The mean values are calculated over the six samples of each mud.

Mud case	ρ (kg/m^3)	τ_B (Pa)	μ_B (Pa s)
Mud_10	1171 ± 0.08%	9.96 ± 0.46%	0.0172 ± 0.67%
Mud_17	1190 ± 0.03%	17.3 ± 0.99%	0.0249 ± 0.63%
Mud_23	1200 ± 0.05%	23.0 ± 1.76%	0.0344 ± 2.56%

remoulded samples (Shakeel et al., 2021). Then, the ramp-down[1] flow curves between 200 and 300 s^{-1} were used for the least-squares fitting of the Bingham model (Fig. 3). For simple shear flow, the Bingham model reads

$$\tau = \tau_B + \mu_B \dot{\gamma}\,, \tag{1}$$

where τ (Pa) is the shear stress, $\dot{\gamma}$ (s^{-1}) is the shear rate, τ_B (Pa) is the Bingham yield stress and μ_B (Pa s) is the Bingham (or plastic) viscosity. The mean density and the mean Bingham parameters (over the six samples) of each mud are reported in Table 2, together with the standard uncertainties that will be used for the estimation of the input parameter uncertainties in the numerical simulations.

2.4. Analysis of experimental data

2.4.1. Calibration uncertainty

The experimental uncertainties were estimated following the procedure in the ISO-GUM (International Organization for Standardization (ISO), 1995). The first source of experimental uncertainty originates from the calibration of the load cell, U_{cal}. The calibration is needed to find the coefficients that ensure the correct conversion of the measured signal from Volt to Newton. This was done by attaching a thread to the plate, and then pulling it in the flow direction with a dynamometer that was previously calibrated using weights. The force was increased from 4 to 24 N by constant increments of 2 N, and the calibration coefficients were obtained from linear curve fitting. Thereafter, the load cell was tested again using the found coefficients, and the maximum observed discrepancy against the dynamometer was about 3.5%. One possible explanation for such rather large discrepancy is that the load cell, which is capable of measuring up to 1000 N, is working in a low range of forces. In fact, the discrepancies between the load cell and the dynamometer were lower when the applied forces were larger. Another reason can be attributed to the non-perfect rigidity of the system composed by the load cell and the plate. Eventually, it was decided to adopt $U_{cal} = 4\%$ as a 'Type B' uncertainty.

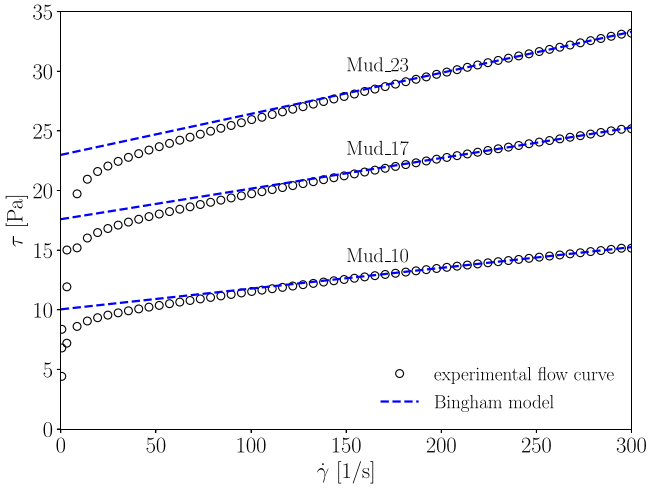

Fig. 3. Ramp-down flow curves and Bingham fits for one of the six samples of each mud.

2.4.2. Repeated tests uncertainty

The uncertainty in the mean force due to the repeated tests can be estimated by statistical methods ('Type A' uncertainty). For a given mud concentration and a given speed, tests were repeated eight times. In order to determine the time window in which the force signal is stationary (see Fig. 4), the Transient Scanning Technique (TST) (Brouwer et al., 2019) was applied using an open source code (Lemaire and Klapwijk, 2021). Some force signals had to be discarded because it was not possible to find any time window in which the signal appeared to be statistically steady. This means that the actual number of repetitions may be eventually equal or less than eight. After having established the

[1] The ramp-down curves were used because, after the mixing, the mud is in a remoulded state.

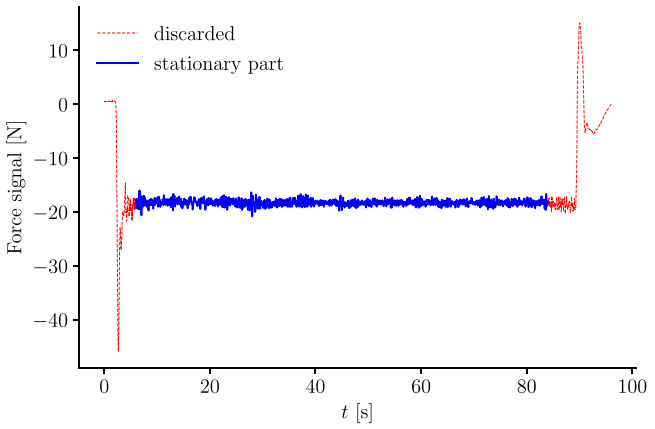

Fig. 4. Instance of one of the force signals obtained at 0.27 m/s with Mud_10. Only the steady part highlighted in the plot was used in Eq. (2).

time interval in which the force signal is stationary, the time-average force $R^i_{t.a.}$ was obtained from each ith signal as

$$R^i_{t.a.} = \frac{1}{n}\sum_{j=1}^{n} f_j\,, \tag{2}$$

where n is the number of sampling data points in the stationary time interval and f_j is the jth sampling force.

The final measured force is the mean of the time-average forces, i.e.

$$R_T \equiv R_{mean} = \frac{1}{N}\sum_{i=1}^{N} R^i_{t.a.}\,, \tag{3}$$

where $N \leq 8$ is the number of repetitions. Then, the (unbiased) standard deviation of the repeated tests reads

$$s = \sqrt{\frac{1}{N-1}\sum_{i=1}^{N}(R_{mean} - R^i_{t.a.})^2}\,, \tag{4}$$

whereas the standard uncertainty is

$$u = \frac{s}{\sqrt{N}}\,. \tag{5}$$

Finally, the expanded uncertainty of the repeated tests is

$$U_{rep} = k\,u\,, \tag{6}$$

where k is the coverage factor. Assuming that the mean force follows the Student's t-distribution, $k = 2.306$ ensures a 95% confidence level with eight repetitions (degrees of freedom). For the cases where some signals had to be discarded, larger coverage factors were used.

2.4.3. Other uncertainties

Other uncertainties such as those due to manufacture tolerances and precision of the measuring devices were assumed to be negligible compared to the calibration and repeated tests uncertainties, therefore they were not considered. Another important source of uncertainty originates from the experimental setup. A way to account for this is to repeat the tests after having disassembled and reassembled the plate, the load cell and the steel beam to which the load cell is attached. In this way, the possible variability in the setup, such as that due to small misalignments of the plate with the carriage direction, would be included in the uncertainties of the repeated tests. However, this was not done as the time required would have been incompatible with the time window available to complete the experiments. As will be shown in Section 4.5, even small rotations of the plate can visibly increase the resistance, thus the experimental uncertainties might have been somewhat underestimated.

Table 3
Mean experimental resistance and relative percentage uncertainty.

V (m/s)	R_T (N)	U_{exp}	R_T (N)	U_{exp}	R_T (N)	U_{exp}
	Mud_10		Mud_17		Mud_23	
0.27	18.0	5.4	30.0	5.3	39.2	4.7
0.52	20.4	4.2	34.2	4.3	44.7	6.2
0.77	23.8	4.2	38.9	4.0	49.0	4.6
1.02	28.3	5.0	45.1	4.6	55.2	4.5

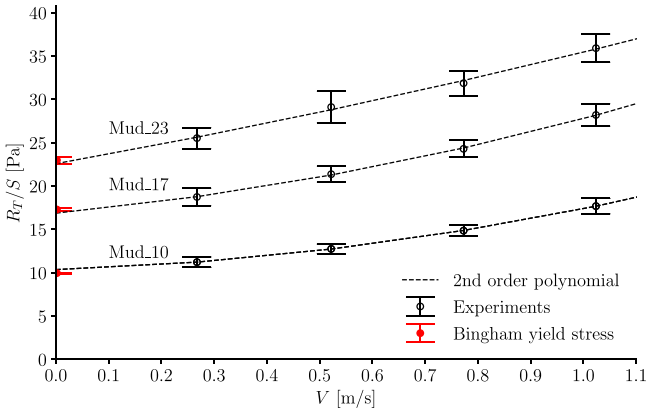

Fig. 5. Extrapolation to $V = 0$ of the experimental resistance (divided by the side surface of the plate) using a second-order polynomial. The Bingham yield stresses are plotted with their standard uncertainties.

2.4.4. Total experimental uncertainty and mean forces

Finally, the experimental uncertainties U_{exp} relative to the mean resistance of the plate were obtained as RMS of U_{cal} and U_{rep}, and are reported in Table 3 together with the mean experimental resistance R_T. As expected, the total resistance increases with speed and it is larger for the higher mud concentrations. It is also worth noticing that $R_T \neq 0$ as $V \to 0$, contrary to what would be expected in Newtonian fluids such as air and water. This is because of the mud yield stress, which approximately increases the resistance by $\tau_B S$, where $S = 2\,L\,T$, with L and T being the plate chord and draught, respectively. In fact, a good estimate of the Bingham yield stress can be obtained by extrapolation to $V = 0$ of R_T/S with a second-order polynomial (Fig. 5). These estimates are within 3% of the Bingham yield stress for the three muds. This is a first indication that, for this application, the rheology of mud is reasonably well captured by the Bingham model. Note, however, that small deflections of the plate might have increased the measured resistance at the higher speeds (this is discussed in Section 4.5). Therefore, results at the higher speeds must be interpreted with caution.

3. CFD setup

The experimental data reported in the previous section have been compared with the predictions obtained with a CFD code, which solves the governing equations of fluid dynamics using numerical methods. This section presents the governing equations, the computational domain, the boundary conditions and it gives an overview of the particular flow solver used for this work. Finally, the numerical and input parameters uncertainties are discussed.

3.1. Governing equations

An important decision that will have significant impact on the computing costs is to whether the free surface must be modelled or not.

In a first crude approximation, the plate can regarded as a marine vessel and the resistance can be divided into a viscous component

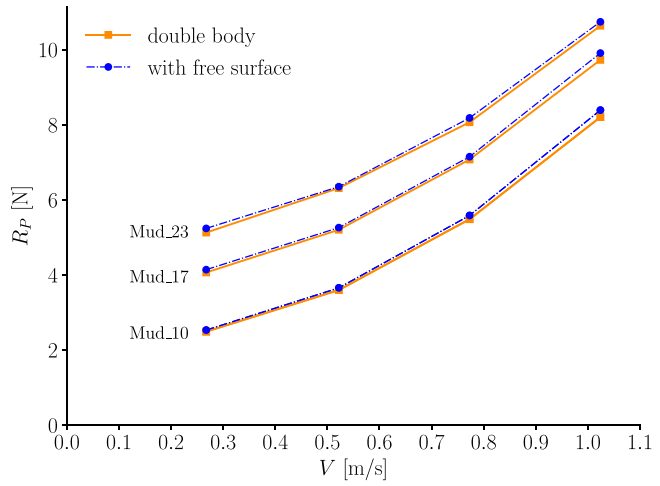

Fig. 6. Pressure resistance computed with and without the free surface (M = 12000, see Section 3.5.2).

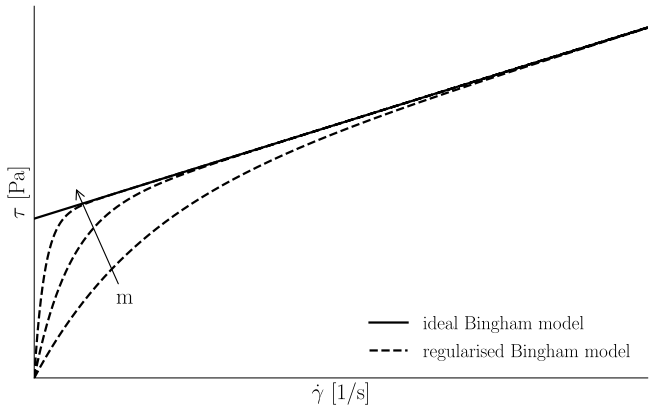

Fig. 7. Effect of the regularisation parameter, m, on the Bingham model for simple shear flow.

and a wave component. The latter can be reasonably considered to be a function of only the Froude number, $F_n = V/\sqrt{gL}$, where V is the speed, g is acceleration of gravity and L is the plate length. The maximum Fn for the plate is 0.36, a value that is typical of fishing vessels. For these type of vessels the wave resistance is roughly 60% of the total resistance (Larsson and Raven, 2010). However, it is possible to identify at least two reasons to neglect the wave resistance for the case of a plate moving in mud.

First, with the given dimensions, the plate has a wetted surface that is roughly ten times that of a fishing vessel, thus the viscous component is also roughly ten times larger. This already reduces the wave expected resistance from 60% to about 15% of the total resistance. Second, even neglecting the yield stress, the least viscous mud (Mud_10) has a viscosity that is about twenty times that of water. Since in laminar regime the drag on a flat plate scales with $\sqrt{\mu_B}$, the viscous resistance in mud is at least four times larger than in water. This brings the expected wave resistance for the highest speed down to only a few percent of the total resistance, meaning that the effect of the free surface could be neglected.

To further validate this assumption, preliminary calculations were performed including the free surface, which was modelled using the Volume-Of-Fluid (VOF) method (Hirt and Nichols, 1981). Simulations were run in unsteady mode and the time integration was performed implicitly with a first-order backwards Euler scheme. The convective flux of the volume-fraction equation was discretised with an interface-capturing scheme (Klaij et al., 2018) and the grid was refined around the initial mud level. Fig. 6 shows that double-body (without free surface) and free-surface calculations produce virtually the same pressure resistance. In terms of the total resistance, the average and maximum difference are 0.3% and 0.9%, respectively, in percentage of the double-body results.

In light of the above considerations, the contribution of the wave resistance can be neglected, thus double-body calculations are performed unless stated otherwise. The equations being solved are the incompressible continuity and momentum equations (in Cartesian coordinates):

$$\nabla \cdot \boldsymbol{u} = 0\,, \tag{7}$$

$$\frac{\partial \rho \boldsymbol{u}}{\partial t} + \nabla \cdot (\rho \boldsymbol{u}\,\boldsymbol{u}) = \nabla \cdot \boldsymbol{\tau} - \nabla p\,, \tag{8}$$

where $\mathbf{u}$ is the velocity vector and p is the pressure. The flow behaviour of mud has been described by the Bingham constitutive equation, for which the deviatoric stress tensor, $\boldsymbol{\tau} \equiv \tau_{ij}$, reads:

$$\begin{cases} \tau_{ij} = 2\left(\dfrac{\tau_B}{\dot{\gamma}} + \mu_B\right) S_{ij} & \text{for} \quad \tau_B \le |\tau_{ij}|\,, \\ S_{ij} = 0 & \text{for} \quad |\tau_{ij}| < \tau_B\,, \end{cases} \tag{9}$$

where $S_{ij} = 1/2(\nabla \mathbf{u} + \nabla \mathbf{u}^T)$ is the deformation rate tensor, $\dot{\gamma} = 2\sqrt{S_{ij}S_{ij}/2}$ and $|\tau_{ij}| = \sqrt{\tau_{ij}\tau_{ij}/2}$.

In order to avoid numerical difficulties caused by the infinite viscosity when $\dot{\gamma} = 0$, the regularisation approach of Papanastasiou (Papanastasiou, 1987) is used, thus the non-differentiable constitutive equation Eq. (9) is replaced by

$$\tau_{ij} = 2\left[\frac{\tau_B(1 - e^{-m\dot{\gamma}})}{\dot{\gamma}} + \mu_B\right] S_{ij}\,, \tag{10}$$

where m is the regularisation parameter. In the limit of $m \to \infty$, Eq. (10) tends to Eq. (9), as shown in Fig. 7. The uncertainties originating from the use of the regularisation are discussed in Section 3.5.2. The term between square brackets in Eq. (10) is often called apparent viscosity, and it reduces to μ_B for Newtonian fluids.

3.2. Force calculations

One of the advantages of numerical methods over the experiments is the possibility to distinguish between the frictional and the pressure resistance. These components are calculated respectively as:

$$R_F = \left(\int_{S_w} \boldsymbol{\tau} \cdot \boldsymbol{n} ds\right)_x\,, \quad R_P = \left(\int_{S_w} -p \cdot \boldsymbol{n}\right)_x ds\,, \tag{11}$$

where S_w is the total wetted surface of the plate, $\boldsymbol{n}$ is the unit normal vector of the plate pointing outwards and the subscript x indicates the x-component (flow direction). The total plate resistance, R_T, is simply the arithmetic summation of R_P and R_F.

3.3. Computational domain and boundary conditions

Although experiments at the higher speed may have been affected by small deflections of the plate, calculations will be initially performed with a plate perfectly aligned with the flow direction. The effect of the rotation will be investigated in Section 4.5.

In light of this, only the starboard side of the domain containing the plate has been modelled due to symmetry. The computational domain has been discretised with H-type grids (Fig. 8). In order to reproduce the experimental setup, two series of grids were generated: one where the plate is immersed in the mud up to 1.0 meter (used for Mud_10 and Mud_17), and another where the plate is immersed up to 0.96 meter (used for Mud_23). For both series, the finest grid is made of about 1.77

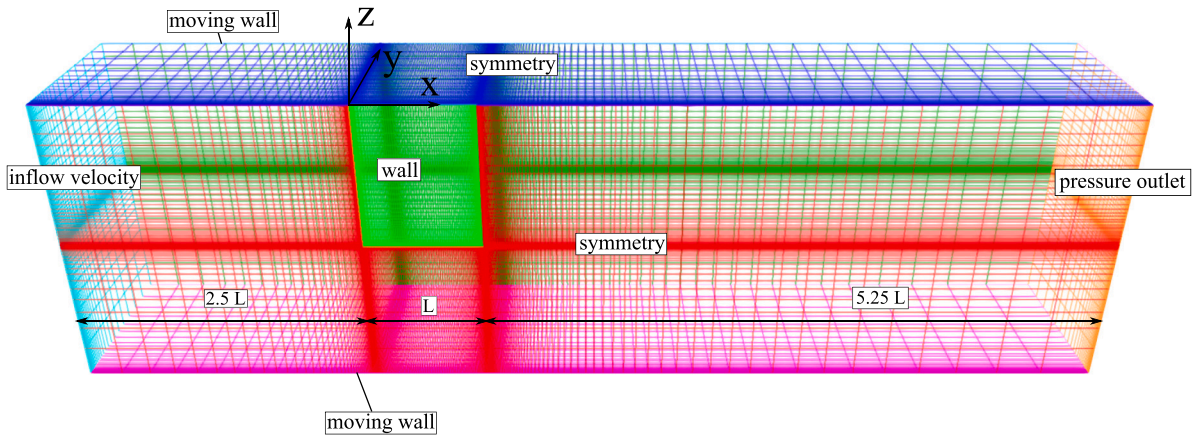

Fig. 8. Computational domain (finest grid) and boundary conditions.

million cells and the size of the first cell away from the plate surface is 2×10^{-4}, yielding the maximum y^+ between 0.6 and 2.4 among all calculations.

For the boundary conditions, the inflow velocity (towing carriage's speed) was applied at the inlet boundary, whereas the no-slip/non-permeability condition was applied to the plate surface (Fig. 8). At the outlet, a Dirichlet condition was imposed for the pressure while symmetry conditions were applied to the top and symmetry plane. The side and bottom boundaries were set as impermeable walls moving at the same velocity of the inflow.

The inlet and outlet boundaries were placed at a distance equal to 2.5 and 5.25 plate lengths, respectively. Calculations performed with twice the distance showed a maximum difference lower than 0.1% in the plate's drag, confirming that the domain is sufficiently long to neglect the influence of the inlet and outlet boundaries.

3.4. Flow solver

The CFD code used for the present work is ReFRESCO (Vaz et al., 2009), a viscous-flow code currently being developed and verified for maritime purposes by the Maritime Research Institute of the Netherlands (MARIN) in collaboration with several non-profit organisations around the world. The code solves incompressible momentum and continuity equations, together with the volume-fraction equation for free-surface calculations. Originally developed for Newtonian fluids, ReFRESCO has been recently extended and verified for flow simulations of Herschel–Bulkley fluids, of which Bingham is a particular case (Lovato et al., 2018, 2021). The code includes a number of other features such as cavitation and turbulence models, even for Herschel–Bulkley fluids (Lovato et al., 2022), however they are not considered in the present work.

Equations are discretised in strong-conservation form with a second-order finite-volume method for unstructured mesh with cell-centred co-located variables (see, e.g., the textbook of Ferziger and Perić (1996)). Mass conservation is ensured with a pressure-correction equation based on a SIMPLE-like algorithm (Klaij and Vuik, 2013). The convective fluxes of the transport equations are linearised with the Picard method and discretised with the Harmonic scheme (van Leer, 1979).

3.5. Numerical uncertainties

For steady flows, numerical errors are usually divided into three components: round-off, iterative and discretisation errors. However, the use of the regularisation for the Bingham model produces additional errors, hereafter labelled as regularisation errors. Present calculations were performed on a double-precision machine, therefore round-off errors are neglected and not further discussed.

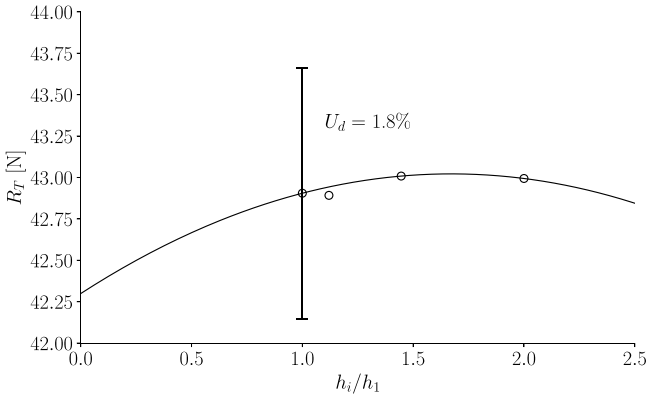

Fig. 9. Grid sensitivity of R_T for Mud_23, $V = 0.27$ m/s. The grid refinement ratios are $h_i/h_1 = 1, 1.12, 1.45, 2$, which correspond to grids having 1.77, 1.26, 0.59, 0.22 millions cells, respectively,.

3.5.1. Iterative and discretisation uncertainties

Iterative errors stem from the use of iterative methods to find the solution of the discretised equations. For this work, the iterative convergence criterion was set to $L_\infty < 10^{-7}$. However, this convergence tolerance was actually hardly met; thus, in practice, iterations were stopped when the maximum number of iterations was reached. As a result, iterative errors could not be neglected and the uncertainties, U_{it}, were estimated using the method of Eça and Hoekstra (2009).

Discretisation errors arise from the use of grids with a finite number of points, and from the use of finite differences instead of partial derivatives. The discretisation uncertainties, U_d, were estimated with the method of Eça and Hoekstra (2014) using four geometrically similar grids. Fig. 9 shows an example of the grid sensitivity of R_T for Mud_23 and $V = 0.27$ m/s.

The iterative and discretisation uncertainties are reported in Table 4 for the pressure, friction and total resistance. The larger percentage uncertainties are found in the pressure component, especially at low speed, with a maximum $U_{it}^P + U_d^P$ of about 16% for Mud_23. For the frictional component, on the other hand, the uncertainties are much lower and do not exhibit a clear trend. Overall, $U_{it}^T + U_d^T$ never exceeds 2.4%.

3.5.2. Regularisation uncertainty

The use of regularisation methods produces an additional error component, the regularisation error, which is the difference between the solution obtained with the regularised and the ideal (non-regularised) model. This error can be minimised by using very large regularisation

Table 4
Iterative and discretisation uncertainties in percentage of the corresponding resistance component for the pressure, frictional and total resistance on the finest grid and keeping the non-dimensional regularisation parameter at $M = 12000$ (see also Section 3.5.2).

V (m/s)	R_P (N)	U_{it}^P	U_d^P	R_F (N)	U_{it}^F	U_d^F	R_T (N)	U_{it}^T	U_d^T
Mud_10									
0.27	2.5	1.4	6.5	17.2	0.0	0.6	19.7	0.1	1.1
0.52	3.6	0.0	2.6	18.0	0.0	1.7	21.6	0.0	0.9
0.77	5.5	0.5	0.7	18.3	0.6	2.7	23.7	0.3	2.0
1.02	8.2	0.1	2.5	18.1	0.7	0.6	26.3	0.1	0.5
Mud_17									
0.27	4.1	1.7	7.1	29.6	0.0	0.1	33.7	0.2	0.8
0.52	5.2	0.0	1.6	31.0	0.0	1.2	36.2	0.0	1.3
0.77	7.1	0.0	2.1	31.7	0.0	0.8	38.8	0.0	0.3
1.02	9.7	0.3	0.8	32.2	0.2	2.6	41.9	0.1	1.9
Mud_23									
0.27	5.1	3.4	13.0	37.8	0.0	0.2	42.9	0.4	1.8
0.52	6.3	4.3	6.0	39.6	0.0	1.2	45.9	0.3	0.4
0.77	8.1	0.0	5.1	40.8	0.0	0.7	48.9	0.0	0.3
1.02	10.6	0.3	0.1	41.6	1.0	0.4	52.3	0.5	0.3

Table 5
Regularisation uncertainties in percentage of the corresponding resistance component for the pressure, frictional and total resistance on the finest grid and $M = 12000$.

V (m/s)	U_{reg}^P	U_{reg}^F	U_{reg}^T	U_{reg}^P	U_{reg}^F	U_{reg}^T	U_{reg}^P	U_{reg}^F	U_{reg}^T
	Mud_10			Mud_17			Mud_23		
0.27	15.0	1.5	3.2	15.8	1.5	3.2	17.6	2.0	3.9
0.52	10.4	1.5	3.0	12.7	1.7	3.2	15.1	2.0	3.8
0.77	6.4	1.3	2.5	9.1	1.5	2.9	10.9	1.8	3.3
1.02	4.2	1.1	2.1	6.3	1.3	2.5	7.7	1.5	2.8

parameters. However, this often leads to slow or stagnating iterative convergence. Furthermore, large regularisation parameters produce stronger viscosity gradients and consequent larger discretisation errors. Because of this interdependency, the final numerical uncertainty was estimated as

$$U_{num} = U_{it} + U_d + U_{reg}\,, \tag{12}$$

where U_{reg} is the regularisation uncertainty.

It is now convenient to introduce $\epsilon = 1/M$, where $M = m\tau_B/\mu_B$ is a non-dimensional regularisation parameter, representing the ratio of the maximum and minimum viscosity attainable by the fluid. In order to estimate U_{reg} one needs to know how the solution varies with ϵ. While this is unknown for the present problem, Frigaard and Nouar (2005) showed that for typical shear flows (like Poiseuille flow) of Bingham fluids, the L_∞ and L_2 error norms of the regularisation errors are $O(\epsilon)$ when using the Papanastasiou regularisation. Thus, in absence of validated methods to estimate U_{reg} from numerical data, it is reasonable to estimate U_{reg} adopting the same method used for U_d, with the grid size replaced by ϵ, as shown in Fig. 10. The uncertainty estimates are reported in Table 5, and they were obtained by varying M between 4000 and 12000. Clearly, the pressure component is (percentage-wise) the most sensitive to the regularisation, especially at low speeds, where U_{reg}^P ranges between 15% and 17.6%.

A possible reason for the strong influence of M on R_P is that M affects the viscosity in low shear rate regions, such as near the stagnation points at the front and rear face of the plate where R_P is generated. In these regions, the pressure increases with M (Fig. 11). On the other hand, in the high shear rate region at the sides of the plate, where the friction component is generated, the viscosity is nearly insensitive to M, explaining the lower sensitivity of R_F. Fortunately, the pressure contribution is small and so the uncertainties in R_T are within 4%.

In conclusion, $M = 12000$ was adopted to mimic the ideal Bingham model.

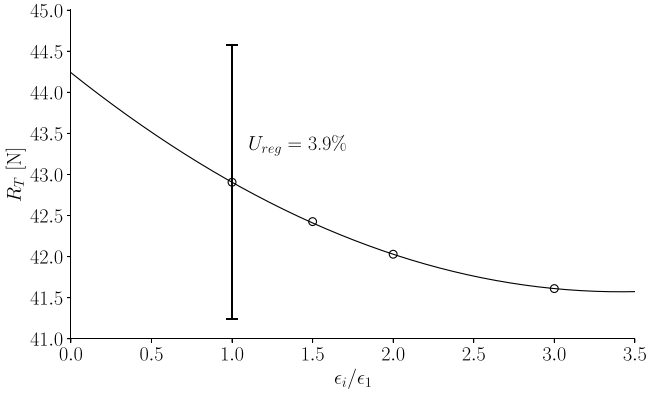

Fig. 10. Sensitivity of R_T to the inverse of the non-dimensional regularisation parameter $\epsilon = 1/M$ for Mud_23, $V = 0.27$ m/s. The refinement ratios are $\epsilon_i/\epsilon_1 = 1, 1.5, 2, 3$, which correspond to M = 12000, 8000, 6000, 4000, respectively.

Table 6
Non-dimensional sensitivity coefficients $\partial R_T/\partial X_i\, \overline{X_i}/\overline{R_T}$ for each input parameter X_i: plate's draught T, carriage's speed V, mud density ρ, Bingham yield stress τ_B and viscosity μ_B. $\overline{X_i}$ is the mean input parameter that is used in the CFD simulations whereas $\overline{R_T}$ is the total resistance from the analytical formulas evaluated for $\overline{X_i}$.

V (m/s)	ρ	T	V	τ_B	μ_B	ρ	T	V	τ_B	μ_B
	Mud_10					Mud_23				
0.27	0.04	1.00	0.10	0.94	0.02	0.02	1.00	0.04	0.97	0.01
0.52	0.12	1.00	0.28	0.83	0.05	0.07	1.00	0.17	0.90	0.03
0.77	0.21	1.00	0.49	0.72	0.07	0.12	1.00	0.30	0.83	0.05
1.02	0.30	1.00	0.70	0.61	0.09	0.18	1.00	0.43	0.75	0.07

3.6. Input parameters uncertainty

Numerical simulations require input parameters that are experimentally determined and that have uncertainties associated with them. The standard input uncertainty, u_{input}, can be calculated using the perturbation method, as

$$u_{input}^2 = \sum_i \left(\frac{\partial R}{\partial X_i} u_i\right)^2, \tag{13}$$

where R is the resistance of the plate, X_i is the ith input parameter, u_i is its corresponding standard uncertainty, $\partial R/\partial X_i$ is the sensitivity coefficient.

For the present work, the input parameters are the following: plate's draught T, carriage's speed V (flow velocity), mud density ρ, Bingham yield stress τ_B and viscosity μ_B. The standard uncertainties associated with the mud properties were reported in Table 2. For T and V, the standard uncertainty could not be estimated with statistical methods, therefore they were both assumed to be 1%. The sensitivity coefficients could be determined from CFD calculations, however this would lead to an unfeasible number of simulations. It was thus decided to approximate the drag force on the plate by modelling CFD data with the analytical formulas that are discussed in Section 5. While there are some discrepancies between these formulas and CFD data, the agreement is deemed sufficient for the purpose of determining the sensitivity coefficients.

The derivation of $\partial R/\partial X_i$ from analytical formulas becomes then a simple yet lengthy task, which was thus carried out with the aid of computer algebra systems. Table 6 shows the non-dimensional sensitivity coefficients of R_T with respect to each input parameter for Mud_10 and Mud_23.

The largest sensitivity coefficient is for the draught T. As expected, it is exactly equal to 1 (i.e. linear relation) since both R_P and R_F are proportional to the plate surface, which is in turn a linear function of T. For all the other input parameters, the coefficients are less than 1, which means that the input uncertainty for R_T grows less than linearly

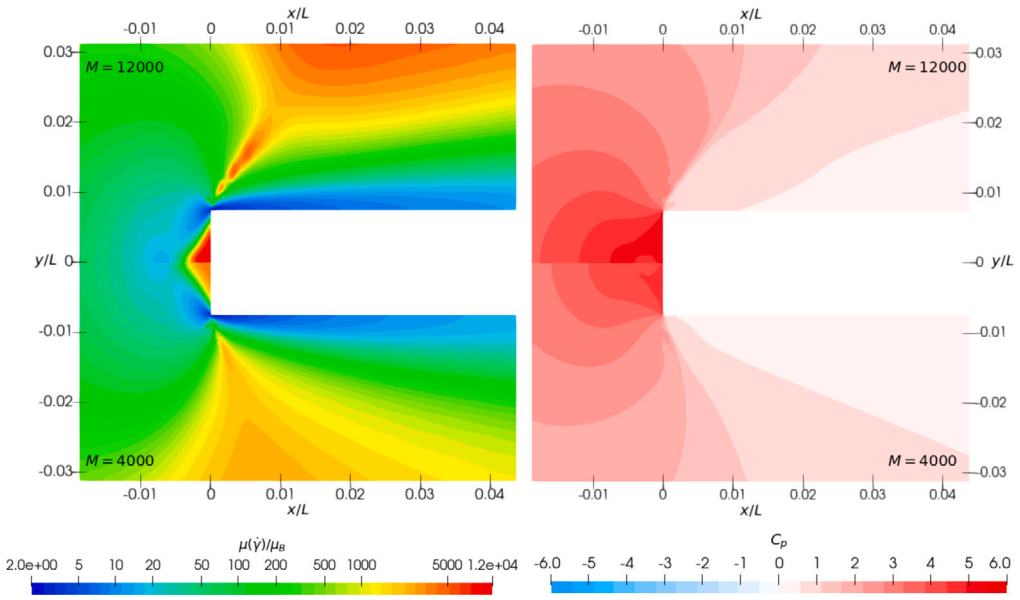

Fig. 11. Effect of regularisation parameter M on the apparent viscosity (left) and pressure coefficient (right) at the leading face of the plate for Mud_23 and $V = 0.27$ m/s. Viscosity is in logarithmic scale. Flow is from left to right. The cutting plane is at $z/T = -0.5$.

Table 7
Input parameter uncertainties in percentage of R_T from CFD ($M = 12000$). The input parameters are the: speed V, plate draught T, mud density ρ and Bingham parameters τ_B and μ_B.

V (m/s)	U^P_{input}	U^F_{input}	U^T_{input}	U^P_{input}	U^F_{input}	U^T_{input}	U^P_{input}	U^F_{input}	U^T_{input}
	Mud_10			Mud_17			Mud_23		
0.27	2.2	2.1	2.1	2.8	2.7	2.7	4.0	3.8	3.8
0.52	2.3	2.2	2.2	2.7	2.6	2.6	3.5	3.7	3.7
0.77	2.2	2.3	2.3	2.6	2.7	2.6	3.3	3.7	3.5
1.02	2.1	2.5	2.4	2.5	2.8	2.6	3.0	3.7	3.5

Table 8
Comparison error, validation uncertainty and modelling errors in percentage of the experimental data. In some cases the sign of the modelling errors could be determined and it is reported between parenthesis.

V (m/s)	E	U_{val}	$\lvert\delta_{model}\rvert \leq$	E	U_{val}	$\lvert\delta_{model}\rvert \leq$	E	U_{val}	$\lvert\delta_{model}\rvert \leq$
	Mud_10			Mud_17			Mud_23		
0.27	9.7	7.6	17.3 (+)	12.3	7.8	20.1 (+)	9.4	9.2	18.5 (+)
0.52	5.6	6.4	12.0	5.8	7.0	12.8	2.6	8.6	11.2
0.77	−0.1	6.8	6.9	−0.2	5.8	6.0	−0.1	6.8	6.9
1.02	−7.1	6.0	13.1 (-)	−7.2	6.7	13.9 (-)	−5.3	6.6	11.8

with an increase of the standard uncertainty. Note, however, that the coefficients in Table 6 are calculated for those particular test cases, therefore different values should be expected for other experimental conditions. Furthermore, the coefficients can be considered accurate as long as the resistance of the plate can be well approximated by the analytical formulas discussed in Section 5. For example, the linear relation between R_T and T is accurate only for small variations of T and, in any case, as long as the shallow water effects remain negligible.

Assuming a Gaussian error distribution, the final expanded input uncertainties are $U_{input} = 2u_{input}$ (95% confidence) and they are reported in Table 7. The largest U_{input} is found for Mud_23 because the latter has the highest uncertainty in τ_B (see also Table 2). Furthermore, U_{input} decreases with V, which reflects the behaviour of $\partial R_T/\partial\tau_B$.

4. Comparison of experimental and CFD data

4.1. Modelling error estimation

According to the validation procedure proposed by ASME (ASME PTC Committee, 2009), the modelling error, δ_{model}, can be estimated by comparing two quantities: the (expanded) validation uncertainty,

$$U_{val} = \sqrt{U^2_{num} + U^2_{exp} + U^2_{input}}\,, \tag{14}$$

and the comparison error,

$$E = S - D\,, \tag{15}$$

where S is the numerical solution value and D is the experimental data. U_{num}, U_{exp} and U_{input} are discussed above.

E and U_{val} define an interval within which δ_{model} falls, i.e.

$$E - U_{val} \leq \delta_{model} \leq E + U_{val}\,. \tag{16}$$

When $|E| \gg U_{val}$, the modelling error can be directly estimated as $|\delta_{model}| \approx |E|$. In all other cases, only the upper and lower bounds of δ_{model} can be determined. If more information about the modelling error is required, the validation uncertainty needs to be reduced.

The estimated δ_{model}, U_{val} and E using the Bingham model with large regularisation parameters ($M = 12000$) are reported in Table 8 in percentage of the experimental value.

At intermediate speeds E is close or within U_{val}, whereas at the lowest and highest speed E tends to exceed U_{val}. In any case, E is never sufficiently larger than U_{val} to allow a direct estimate of δ_{model}. In other words, for all the cases, only the upper bound of the modelling error could be estimated and, for a few cases, also the sign of the error could be determined.

The largest upper bounds of the modelling errors are found at the lowest speed for all three muds, which are also the cases with the largest E. The lowest upper bound of the modelling errors is found for $V = 0.77$ m/s because E is very small for all the three mud concentrations. At this speed, there is an intersection of the numerical and experimental data (see Fig. 12).

The two main observations from Fig. 12 are: (i) the variation of resistance due to the changes of mud rheology is well captured by CFD; (ii) the slopes of the experimental and CFD curves are visibly different. The first observation suggests that the Bingham model is suitable, at least, to study how R_T changes in response to variations of the mud concentration. About the second observation, CFD tends to over-predict R_T at low speed and to under-predict it at high speed. This trend

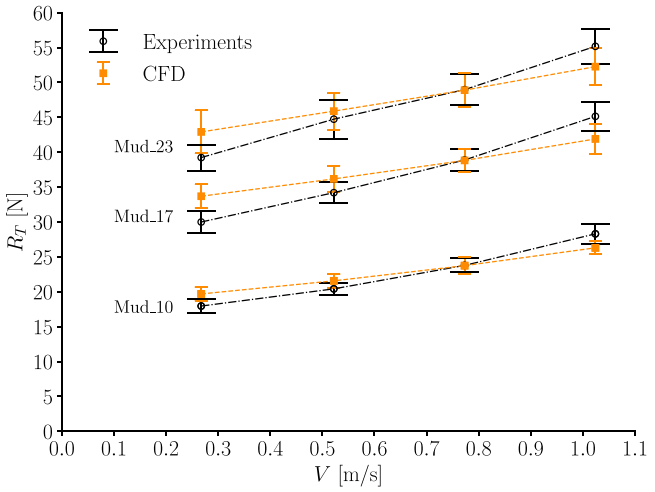

Fig. 12. Total resistance of the plate moving through mud as a function of the inflow velocity. CFD error bars include numerical and input parameter uncertainties. CFD data were obtained keeping the non-dimensional regularisation parameter at $M = 12000$ (see also Section 3.5.2).

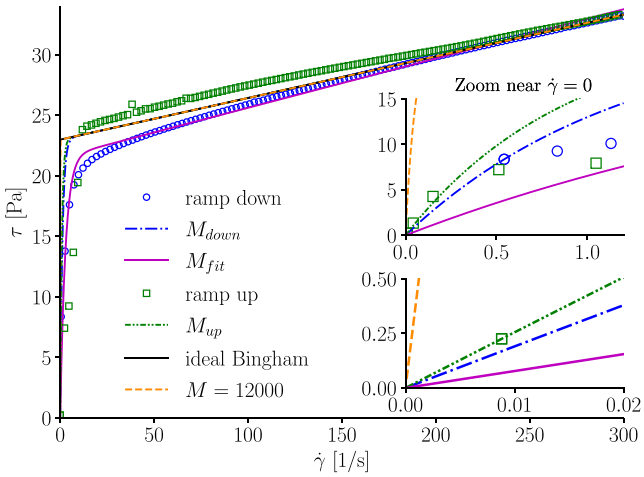

Fig. 13. Regularised Bingham model using different regularisation parameters: $M = 12000$, M_{down}, M_{up} and M_{fit}. The flow curves are for Mud_23.

suggests that E will increase in magnitude for speeds outside the range considered in this work. Some possible causes for this may be the:

- choice of the regularisation parameter
- selected shear rate range for the rheological characterisation of mud
- poor fitting of the Bingham model to the flow curves at low shear rates (see e.g. Fig. 3)
- contamination of experimental data by undesired effects

These possible causes are discussed below.

4.2. Effect of the regularisation parameter

It was just shown that the largest discrepancies between experiments and CFD are found at the lowest speed for all the three mud conditions. Since lower speeds are related to lower shear rates, a possible explanation for this may be the poor modelling of mud at low shear rates. Experimental evidence (e.g. Dzuy and Boger (1985), Ellwood et al. (1990)) suggested that most real fluids do not exhibit an actual yield stress and that regularised models may better capture the behaviour of non-Newtonian materials at low shear rates.

In light of this, it is now questioned whether the rheology of mud may be better described using lower regularisation parameters. A natural choice could be to determine the regularisation parameter, m, from the rheological data. Among the many possible choices, three procedures to determine m are considered:

- M_{down}: m is chosen such that the regularised curve will intersect the first point in the ramp-down flow curve, i.e.

$$m = -\ln\left(1 + \frac{\mu_B \dot{\gamma}' - \tau'}{\tau_B}\right)\frac{1}{\dot{\gamma}'}, \tag{17}$$

  where the prime symbol indicates the first point in the (ramp-down) flow curve. Note that τ_B and μ_B do not change as they are determined from the least-square fitting of the ideal Bingham model (see also Section 2.3).
- M_{up}: m is also obtained from Eq. (17) but using the ramp-up curve.
- M_{fit}: the triplet (m, τ_B, μ_B) is obtained by least-square fitting of

$$\tau = \tau_B(1 - e^{-m\dot{\gamma}}) + \mu_B\dot{\gamma} \tag{18}$$

  to the ramp-down curve.

Table 9
Mean values (± standard uncertainty) of the non-dimensional regularisation parameters obtained from the rheological data. The velocity is in SI units.

V (m/s)	M_{up}	M_{down}	M_{fit}
Mud_10	538 ± 5.7%	687 ± 1.3%	236 ± 1.8%
Mud_17	708 ± 1.8%	658 ± 0.3%	224 ± 1.2%
Mud_23	747 ± 13.3%	556 ± 1.1%	191 ± 1.7%

M_{down} and M_{up} ensure that the regularised Bingham model produces the same apparent viscosity observed in the first point of the ramp-down and ramp-up flow curves, respectively. An alternative procedure similar to M_{down} and M_{up} would be to extrapolate the apparent viscosity to $\dot{\gamma} = 0$ and then use the extrapolated value to derive the regularisation parameter. The latter procedure would be less susceptible to the noise in the first point of the rheological data.

The Bingham fits obtained using the three procedures above are illustrated in Fig. 13, whereas the non-dimensional regularisation parameters are reported in Table 9.

Note that since m is now determined from the mud rheology, the regularisation uncertainty must be estimated as an input parameter uncertainty,

$$U_{reg} = k\, u_{reg} = k\,\frac{\partial R}{\partial m} u_m, \tag{19}$$

where R is the resistance. u_m is the standard uncertainty for six repetitions (number of mud samples) and $k = 2.447$ with 95% confidence assuming a Student t-distribution. The derivative in Eq. (19) is unknown, thus it was approximated with a second-order accurate finite difference,

$$\frac{\partial R}{\partial m} \approx \frac{R(m + u_m/2) - R(m - u_m/2)}{u_m}, \tag{20}$$

where the two terms at the numerator were determined from numerical simulations for each mud condition and speed. For most of the test cases, we found that the regularisation uncertainties have been reduced compared to the calculations with $M = 12000$.

The closest fit to the ramp-down curve is obtained with M_{fit}, whereas M_{up} and M_{down} tend to over-predict the shear stress in the low shear rate range (Fig. 13). However, these observations are not reflected by the accuracy in the force prediction. Fig. 14 shows in fact that M_{fit} produces by far the worst agreement to experimental data, whereas M_{up} and M_{down} produce fairly good predictions at the lower speeds. In particular, M_{up} seems to capture very well the trend at low speeds. At $V = 0.27$ m/s, the comparison error, E, reduces to 1.1%, 0.9% and 4.9% for Mud_10, Mud_17 and Mud_23, respectively. Except for Mud_23, M_{down} and M_{up} produce nearly the same results.

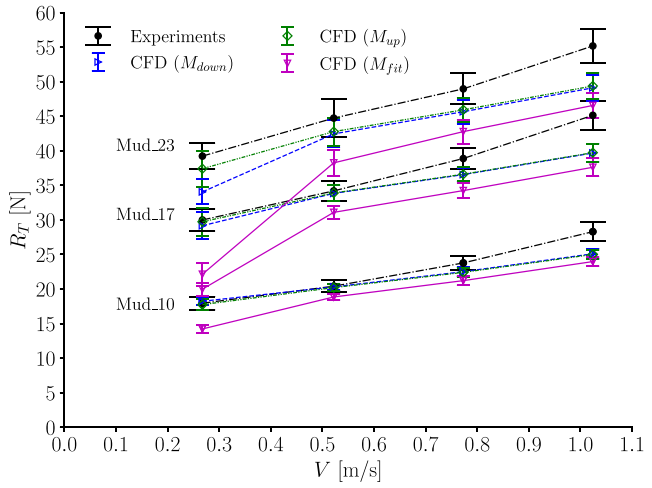

Fig. 14. Effect of different regularisation parameters on the CFD predictions of the plate resistance.

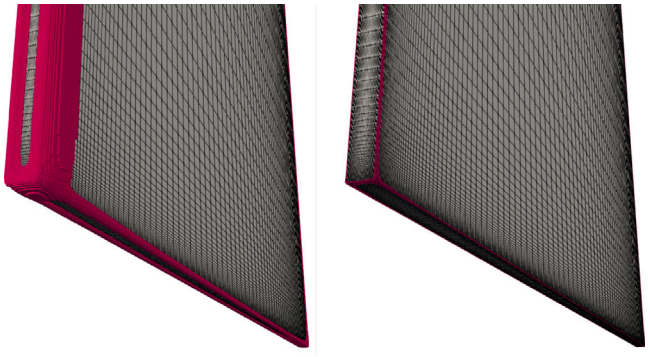

Fig. 15. Highlighted in magenta are the cells where $\dot{\gamma} \geq 300\ s^{-1}$ for Mud_23 near the leading and bottom edge of the plate. $V = 1.02$ m/s (left); $V = 0.27$ m/s (right). (For interpretation of the references to colour in this figure legend, the reader is referred to the web version of this article.)

In conclusion, although the fit using M_{fit} appears closer the mud flow curves, it gives by far the worst numerical prediction. On the other hand, determining the regularisation parameter based on the first points in the flow curves seems to give good agreement with experimental data at low speed. However, the discrepancies become larger at the higher speeds.

4.3. Effect of the shear rate range for the rheology characterisation

Despite the improvements observed at low speeds when the regularisation parameter is determined from the mud rheology, the discrepancies at high speed remain large (even larger than the case with $M = 12000$). Since higher speeds are related to higher shear rates, a possible explanation may be sought in the shear rate range considered for the rheological experiments.

Fig. 15 highlights the fluid regions where the shear rate is above 300 s^{-1}, the latter being the maximum shear rate reached in the rheological measurements. These regions are located near the plate edges, where the fluid experiences strong accelerations. As expected, the case at the higher speed has larger fluid regions with $\dot{\gamma} \geq 300\ s^{-1}$. It is possible that fitting the Bingham model to the flow curve up to 300 s^{-1} is insufficient to accurately predict the force at high speeds (shear rates). Since rheological data for $\dot{\gamma} > 300\ s^{-1}$ are not available, the Bingham parameters corresponding to flow curves with higher $\dot{\gamma}$ have been obtained by extrapolation. Basically, the Bingham parameters were

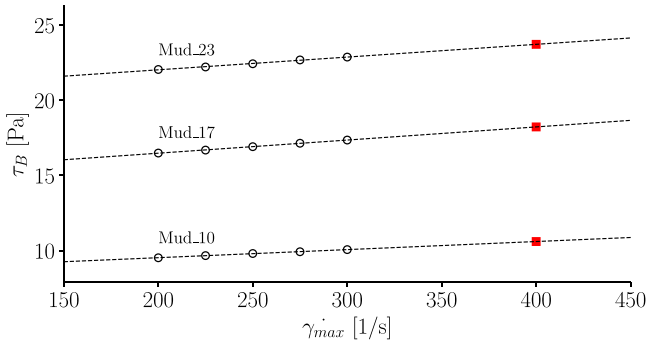

Fig. 16. Bingham yield stresses, τ_B, obtained using different shear rate intervals having $\dot{\gamma}_{max}$ as maximum (open circles); linear fitting of τ_B values for $\dot{\gamma}_{max} \leq 300\ s^{-1}$ (dashed lines); extrapolated τ_B for $\dot{\gamma}_{max} = 400\ s^{-1}$ (filled squares).

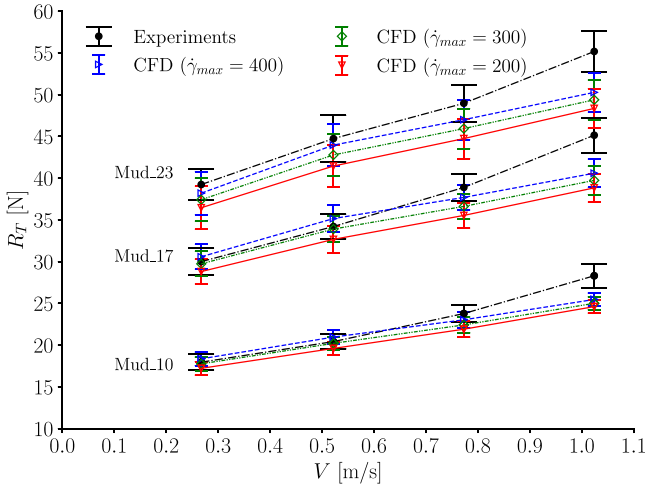

Fig. 17. Effect of the maximum shear rate in the rheology characterisation on the CFD predictions of the plate resistance.

obtained by varying the maximum shear rate,[2] $\dot{\gamma}_{max}$, between 200 and 300 s^{-1}. Then, the Bingham parameters were linearly[3] extrapolated up to $\dot{\gamma}_{max} = 400 s^{-1}$, as illustrated in Fig. 16 for τ_B. It was observed that τ_B increases with $\dot{\gamma}_{max}$, whereas μ_B decreases (not shown).

Numerical simulations were performed for the case M_{up} as an example, which was observed to produce good agreement with experiments at low speed but larger discrepancies at high speed (see Section 4.2). Note that the values of M_{up} are not the same as in Table 9 because the Bingham parameters have changed.

Fig. 17 shows that increasing $\dot{\gamma}_{max}$ seems to slightly improve the agreement with experimental data. This is because higher $\dot{\gamma}_{max}$ gives higher τ_B, which shifts up the CFD data. However, the slopes of the CFD curves are still visibly different from the experimental ones. This is because the slopes of the CFD curves are related to μ_B, but the latter has a rather small influence on the resistance (see also Table 6).

In conclusion, while increasing the maximum shear rate in the rheological tests leads to slightly better agreement with experimental data, it does not explain the discrepancies at the higher speeds.

4.4. Effect of using a more complex rheological model

Can the CFD predictions become more accurate by simply improving the fit of the rheological model to the flow curves? We showed that

[2] The interval used for the Bingham fitting is [$\dot{\gamma}_{max}$ -100s^{-1}, $\dot{\gamma}_{max}$]

[3] It is implicitly assumed that the ramp-down curve will continue up to $\dot{\gamma} = 400 s^{-1}$ without major changes.

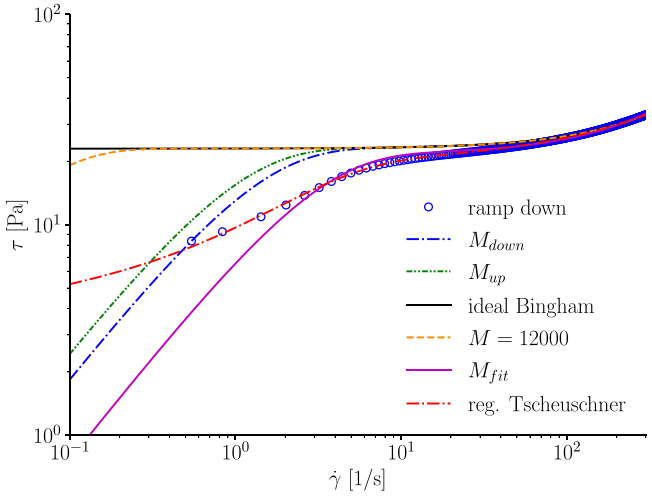

Fig. 18. Comparison of the Bingham and Tscheuschner models for one (ramp-down) flow curve of Mud_23.

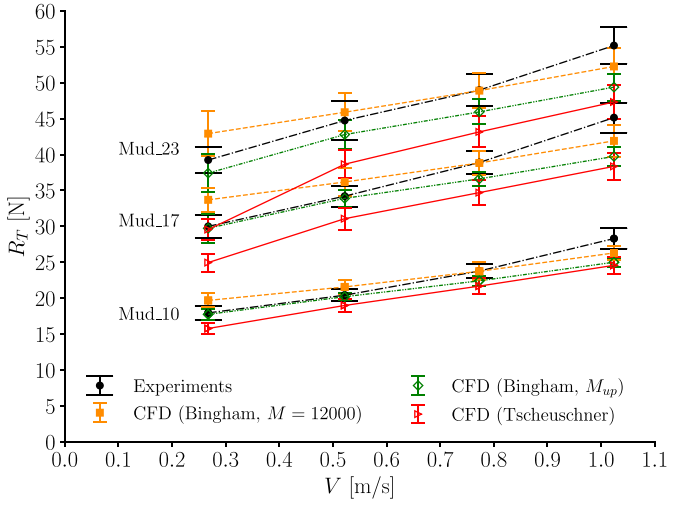

Fig. 19. Total resistance using the Bingham and Tscheuschner model. The Tscheuschner uncertainty bars are set to 5% as a reference.

Table 10
Mean values (± standard uncertainty) of the Tscheuschner parameters.

Mud case	τ_0 (Pa)	m (s)	μ_1 (Pa s)	μ_2 (Pa s^n)	n
Mud_10	3.61	0.433	0.0146	3.97	0.103
Mud_17	8.07	0.372	0.0249	5.48	0.112
Mud_23	12.06	0.322	0.0295	6.34	0.118

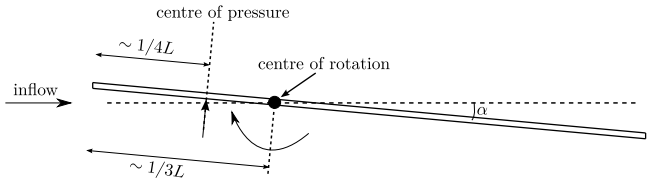

Fig. 20. Schematic representation of the mechanism responsible for the possible increased rotations of the plate at the higher speeds.

M_{fit} gives the closest fit to the ramp-down curve while producing the worst resistance prediction. This is now further investigated using the regularised Tscheuschner rheological model (Mezger, 2020), which can be adjusted to be a virtually perfect fit of the ramp-down flow curves (Fig. 18). This model was originally developed for chocolate and it provides a somewhat mixed behaviour of Bingham and Herschel–Bulkley fluids. For simple shear flows, the model reads

$$\tau = \tau_0\left(1 - e^{-m\dot{\gamma}}\right) + \mu_1\dot{\gamma} + \mu_2\dot{\gamma}^n, \tag{21}$$

where μ_1 and μ_2 determine the slope of Eq. (21) at high and low shear rates, respectively. The quintuplet (m, τ_0, μ_1, μ_2, n) was obtained by least squares fitting of Eq. (21) to the ramp-down curve of the six mud samples, and the mean values (reported in Table 10) were fed to the CFD solver.

In spite of its excellent fit to the flow curves, the Tscheuschner model produces strong underestimations of the resistance (Fig. 19), especially at low speed. At the higher speed, the Tscheuschner model tends to produce the same results as the Bingham model with M_{up}. The maximum and minimum comparison errors among all cases are respectively 13% and 25%. The reasons for the poor predictions of the Tscheuschner model despite being an excellent fit of the ramp-down flow curves are not clear. However two possible explanations are given.

First, the protocol used for the rheological experiments may not be accurate enough at low shear rates. Thus, capturing the ramp-down flow curve down to the lowest value of $\dot{\gamma}$ may give worse numerical predictions simply because of inaccuracies in the flow curves. Second, a possible reason can be the thixotropy of mud. Although the mud was heavily mixed prior the experiments, a partial structural recovery has certainly occurred during the tests, thus the ramp-down may not be a very accurate representation of the flow behaviour of mud, in particular at low speeds/shear rates. Using thixotropic models may help in this regard. On the other hand, the Bingham model, which fits the ramp-down flow curve only in the higher shear rate range, seems to be somewhat between the ramp-up and ramp-down curves (see Fig. 13), which may be an acceptable compromise for high-shear flows.

4.5. Effect of non-zero angles of attack

Another possible explanation for the discrepancies at high speed could be sought in the experimental data rather than in the rheological model.

The alignment of the plate with the flow direction is one of the main challenges when performing towing experiments. While the increase in resistance due to small misalignments may be negligible with low velocities, it could become substantial at higher speeds. In fact, increasing the angle of attack mainly increases the pressure resistance, which is proportional to V^2. In turn, stronger pressure disturbance can also increase the wave resistance. Furthermore, for the present experiments, the load cell was attached to the plate at about $1/3L$ from the leading edge (Fig. 20). But the centre of pressure for flat plates is approximately at $1/4L$ from the leading edge, meaning that an initially small angle of attack could have been amplified at higher speeds. The magnitude of this amplification depends upon the rigidity of the mechanical system formed by the plate and the load cell.

Unfortunately, the angle of attack is not known, thus correcting experimental data for this effect is not possible. Nevertheless, the effect of the plate rotation can be modelled numerically to verify whether the trend of the experimental data can be better captured.

Calculations were thus performed after applying a grid deformation (rotation around the z-axis). Since the rotation of the plate can increase the wave resistance, calculations were performed including the free surface, with the same settings as in Section 3.1. Obviously, since the problem is no longer symmetrical, calculations were performed on the full domain instead of half, as shown in Fig. 21.

It is remarked that the uncertainties in the CFD data are no longer known both because the input uncertainties cannot be simply determined from analytical formulas (as was done in Section 3.6) and because performing a grid/regularisation refinement study for these computations was deemed outside of the scope of the present

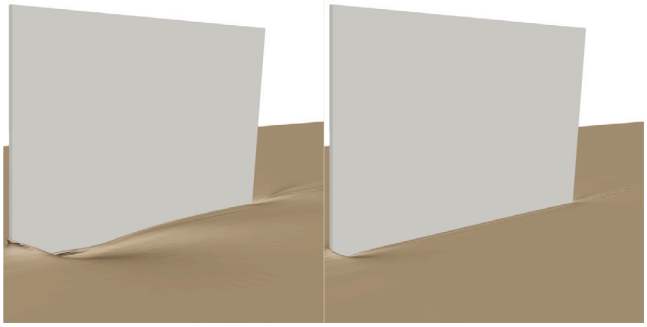

Fig. 21. Simulated mud free surface for Mud_10 at V=1.02 (left) and 0.52 m/s (right). Both simulations are with an angle of attack of 3 degrees and $M = 12000$. Flow is from left to right.

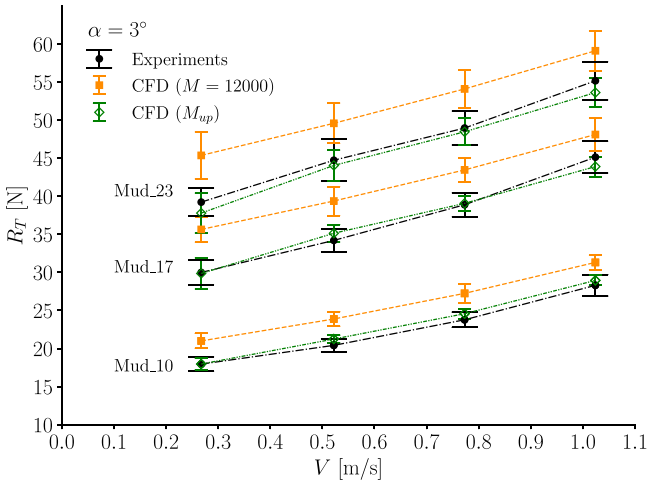

Fig. 22. Resistance of the plate moving through mud. CFD data are obtained with an angle of attack of 3 degrees and including the effect of the free surface. CFD uncertainties are relative to the analogous double-body calculations with zero angle of attack.

study. As reference, the uncertainties from the analogous double-body calculations with zero angle of attack are shown.[4]

Although the actual angle of attack is unknown, an angle between 1 and 5 degrees appears to be reasonable choice since, with larger angles, the deflection would have likely been detected during the experiments, even by the naked eye. In light of this, the effect of an angle of attack of 3 degrees on the resistance is illustrated in Fig. 22 for the cases M_{up} and $M = 12000$. Interestingly, the trend of the experimental data is now well predicted by CFD. In particular, M_{up} almost duplicates the experimental data, whereas the ideal Bingham model ($M = 12000$) captures the trend of the experimental data but it visibly over estimates the resistance.

It is thus inferred that experimental data at the highest speeds are likely contaminated by a rotation of the plate. This also suggests that lower regularisation parameters (e.g. M_{up}) produce better prediction than the ideal Bingham model, which tends to over-estimate the total resistance.

The difference in the predictions between M_{up} (low regularisation parameter) and $M = 12000$ (very high regularisation parameter) is mainly due to the pressure component. In particular, this appears to be related to the larger viscosity in the low deformation regions (i.e where the regularisation is activated), as for example at the rear stagnation point (Fig. 23, left panel). For $M = 12000$, such high viscosity leads to higher pressure on the right surface (pressure side) and to lower pressure on the left surface (suction side) compared to M_{up} (Fig. 23, right panel). Similar observations were also made above when analysing the regularisation uncertainty.

4.6. Final remarks on the regularisation parameter and proposed rule of thumb

We recall that the general rule when using regularisation methods is to use the highest possible regularisation parameter in order to mimic the ideal model as closely as possible. This approach, however, can lead not only to larger discrepancies with experimental data (see Section 4.2) but also to numerical difficulties, such as stagnating or even diverging residuals in the iterative solver.

It was shown that these issues can be mitigated by using lower regularisation parameters based on the first point in the flow curves. Although this procedure is purely empirical and no physical explanations were provided, a general rule of thumb could be devised. In fact, for all the mud conditions considered in this work, the non-dimensional regularisation parameters obtained from the first point in either the ramp-up (M_{up}) or ramp-down (M_{down}) were between 538 and 747. A reasonable rule of thumb to choose the regularisation parameter is thus $M = m\tau_B/\mu_B \approx 800$. This means that the mud apparent viscosity in low-deformation regions is about 800 times the viscosity of mud in the high shear rate regions (e.g. boundary layers). Further research is needed to verify the applicability of such an empirical approach to other test cases.

5. Comparison of CFD data with analytical formulas

The frictional component of the total resistance, R_F, originates from the shear stress acting on the side surfaces of the plate. These surfaces can be approximated as flat plates. A friction coefficient for laminar Bingham flows over flat plates was derived by Chhabra and Richardson (2008) using a third degree polynomial approximation for the velocity profile:

$$C_{RF} \equiv \frac{R_F}{1/2\rho V^2 S} = \frac{1.292}{\sqrt{Re}} + Bn, \tag{22}$$

where $Re = \rho V L/\mu_B$ is the Reynolds number and $Bn = \tau_B/(1/2\rho V^2)$ is the Bingham number. S is the surface of the flat plate that, for the present work, is $2\,L\,T$. Eq. (22) is identical to its Newtonian counterpart when $Bn = 0$. Therefore, we propose a slightly different version that reduces to the well-known Blasius formula when $Bn = 0$, i.e.

$$C'_{RF} = \frac{1.328}{\sqrt{Re}} + Bn. \tag{23}$$

The comparison of Eq. (23) with CFD data is plotted in Fig. 24. At the lower speeds, the agreement is excellent, with an average difference of about 2% relative to CFD. On the other hand, the agreement seems to deteriorate at higher speeds. In particular, the numerical predictions appear to decrease with speed, which may be surprising. However, this can be explained by the presence of a recirculation region near the leading edge (Fig. 25). In this region, the velocity is relatively low, leading to lower shear rate (and consequently shear stress) at the wall. As expected, we found that the recirculation region is larger for Mud_10, which is the least viscous mud.

For the case of a ship moving through mud, Eq. (23) shows that (for laminar mud flow) the increase in frictional resistance due to the yield stress is well approximated by $\tau_B S_{mud}$, where S_{mud} is the surface area of the hull in contact with mud. In case of turbulent flow, however, direct numerical simulation on pipe flows (Rudman and Blackburn, 2006; Singh et al., 2017) showed that a drag reduction is actually expected

[4] The actual uncertainties are likely larger than those of the double-body calculations because of the additional discretisation errors produced by the volume-fraction equation.

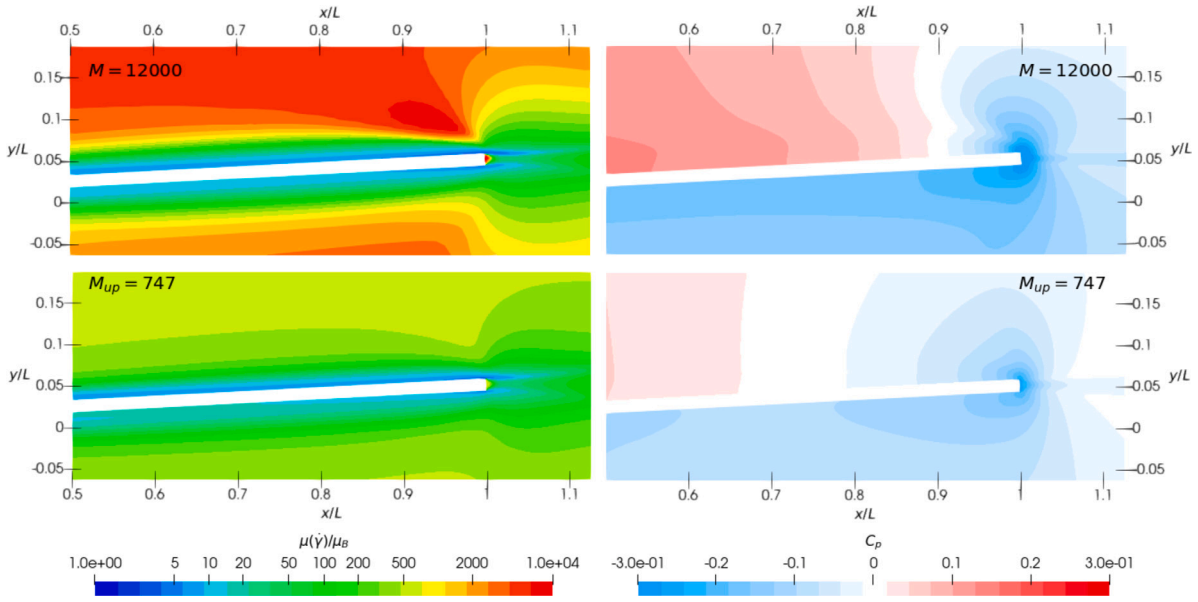

Fig. 23. Contour diagram at the rear part of the plate with an angle of attack of 3 degrees. Apparent viscosity (left); hydrodynamic pressure coefficient (right). The cutting plane is at $z/T = -0.5$ (T is the plate's draught) and the test case is Mud_23, $V = 1.02$ m/s.

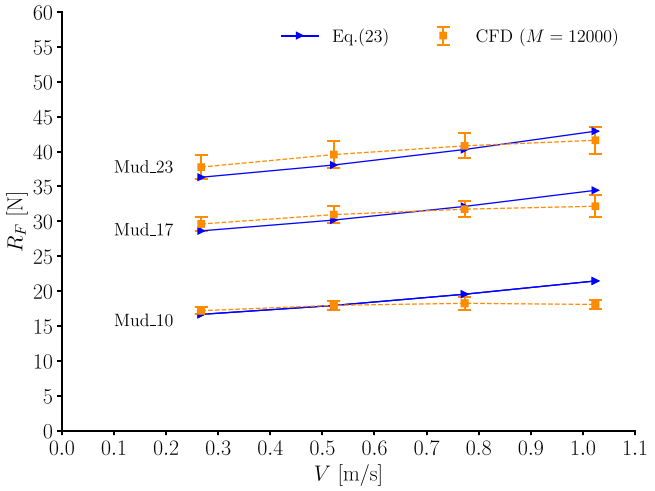

Fig. 24. Comparison of the frictional resistance obtained with Eq. (23) and CFD using large regularisation parameters ($M = 12000$).

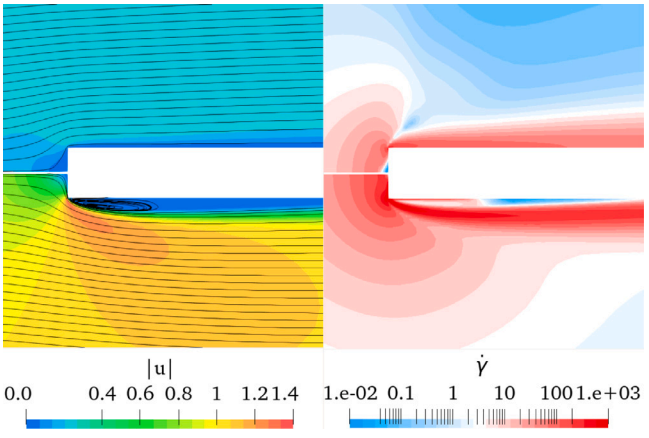

Fig. 25. Contour diagram of velocity (left) and shear rate (right) near the leading edge for Mud_10 ($M = 12000$). Lowest speed (top); highest speed (bottom). Shear rate is in logarithmic scale.

with increasing yield stress. In this case, $\tau_B S_{mud}$ can still be used as an upper bound.

The pressure component, R_P, originates from the pressure difference acting on the front and rear faces of the plate. For Newtonian fluids it may be reasonable to simply use the stagnation pressure applied over the front surface. However, the yield stress influences the pressure significantly, thus this is a too crude approximation.

A possible alternative would be to use the formula proposed by Nirmalkar et al. (2013) for the pressure resistance coefficient, C_{RP}, based on CFD simulations of the Bingham laminar flow over a square cylinder:

$$C_{RP} \equiv \frac{R_P}{1/2\rho V^2 S_f} = \frac{27}{Re_*}, \tag{24}$$

where $S_f = tT$ is the projected frontal area of the cylinder, $Re_* = Re/(1 + Bn*)$ is the modified Reynolds number and $Bn^* = \tau_B L/(\mu_B V)$ is the canonical Bingham number. The conditions of the present work, however, differ from those in Nirmalkar et al. (2013). First, Eq. (24) was derived for $0.1 < Re < 40$, whereas for our test cases $7500 < Re < 56000$. Second, the plate has an aspect ratio of about 66.7 instead of 1.

It was thus decided to use instead the following cubic relation in logarithmic scale:

$$\log_{10}(C_{RP}) = \log_{10}(k_1) + k_2 \log_{10} Re_* + k_3(\log_{10} Re_*)^2 + k_4(\log_{10} Re_*)^3, \tag{25}$$

where $k_1 = 41.58$, $k_2 = -1.132$, $k_3 = 0.1148$ and $k_4 = 0.0313$ are the fitting parameters obtained by least-square fitting of Eq. (25) to the present CFD data ($M = 12000$) for C_{RP}. Eq. (25) corresponds, in linear scale, to

$$C_{RP} = k_1 Re_*^{k_2 + k_3 \log_{10} Re_* + k_4(\log_{10} Re_*)^2}. \tag{26}$$

Fig. 26 shows that Eq. (26) is an excellent fit of the CFD data, with a maximum difference of 0.42%. Furthermore, while Eq. (24) may still be acceptably accurate for low Re_* (low speed, high mud concentration), it is not adequate at higher Re_*, where the simple stagnation pressure applied to the front face of the plate ($C_{RP} = 1$) appears to be closer to CFD data.

The total resistance obtained combining Eqs. (23) and (26) agrees well with CFD data (see Fig. 27), with larger discrepancies at higher speeds stemming from the frictional component. In conclusion, the analytical formulas provide reasonably good estimates of R_T, with

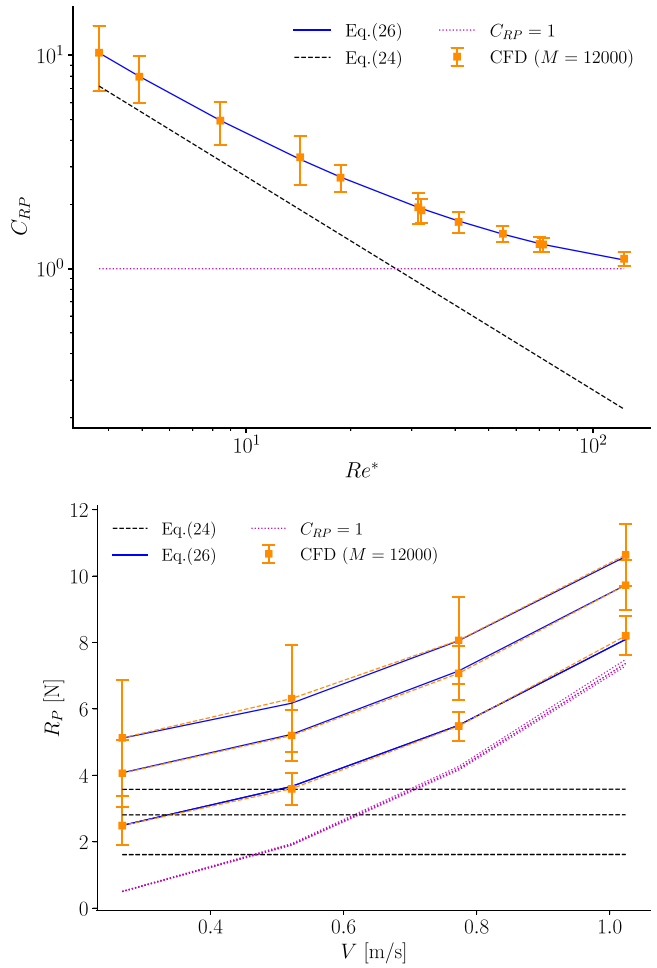

Fig. 26. Pressure resistance coefficients versus the modified Reynolds number (top) and pressure resistance versus speed (bottom).

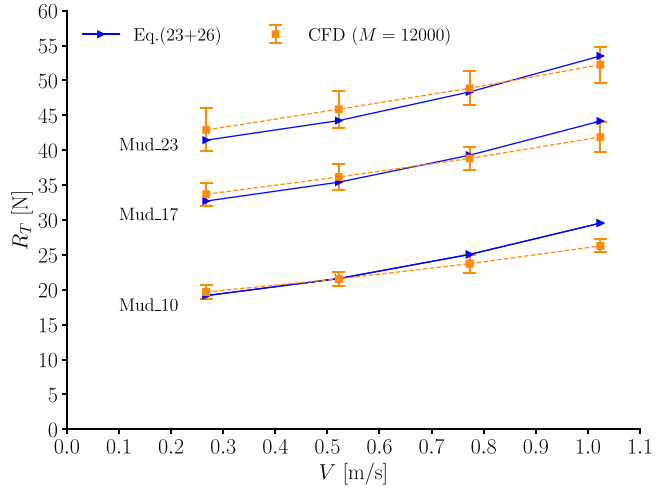

Fig. 27. Comparison of the total resistance predicted by analytical formulas and CFD data.

average and maximum difference of 3.6% and 12.4%, respectively, relative to CFD.

Finally, since the trend of the CFD data is reasonably well captured, Eqs. (23) and (26) have been used to determine the sensitivity coefficients for the input parameter uncertainties (see Section 3.6).

6. Conclusions

We have investigated the accuracy of the Bingham model for CFD applications concerned with marine vessels sailing through fluid mud. As a simplified case, the laminar flow over a plate was considered in order to primarily investigate the influence of the mud properties on the frictional part of the resistance.

The comparison with experimental data showed that the ideal Bingham model ($M = 12000$) well captures the relative increase of the resistance due to the increase of mud concentration. On the other hand, at low speed (i.e. low shear), the ideal Bingham model tends to over-predict the resistance. Better predictions at low speed were achieved by using lower regularisation parameters ($500 < M < 800$), determined from the first points in the mud flow curves.

It was observed that the Tscheuschner model, which is a virtually perfect fit of the ramp-down flow curves of mud, produced strong under-predictions of the resistance, especially at low speed. The reasons might be the thixotropy of mud and possible inaccuracies of the rheological protocol at low shear rates. The main message is that improving the fit of the ramp-down curve does not necessarily lead to better numerical predictions of the plate resistance. In this regard, further research is needed to investigate whether thixotropic models would improve the numerical predictions.

In addition, it was observed that the computed forces can be fairly well approximated by simple analytical formulas. This allowed to quantify the influence on the resistance of each input parameter.

We found convincing indications that experimental data at high speed have been affected by unwanted non-zero angles of attack of the plate. When an angle of attack of 3 degrees was included in the CFD calculations, the trend of the experimental data was very well captured. Therefore, the experimental results need to be interpreted with due caution. Further work is recommended to provide new experimental data with higher rigidity and a better alignment of the plate. Nonetheless, the following observations were made:

- The ideal Bingham model ($M = 12000$) tends to over-predict the experimental data, with an average and maximum comparison error of 13 and 19%, respectively. Nevertheless, the model appears suitable, at least, to investigate how the resistance changes in response to changes in the mud properties.
- Using lower regularisation parameters ($500 < M < 800$) produces better predictions, with comparison errors that are within or close to the validation uncertainties. A possible rule of thumb to select the regularisation parameter could thus be $M \approx 800$.

The generalisation of these results is subject to a number of limitations related to the mud. First, towing tank experiments were conducted on dilutions of the natural mud collected in the harbour area. However, diluted and natural mud can exhibit different rheological characteristics (Shakeel et al., 2020c). Second, this study was limited to three mud conditions, thus our findings cannot be extrapolated to all types of mud. Future studies with other mud conditions would be interesting.

As the flow was assumed to be laminar, it can be argued that this study is valid for the case of a ship moving very slowly through mud (e.g. while docking). However, in the turbulent regime, the non-Newtonian effects would reduce, thus the choice of the rheological model would become even less important. In other words, if the Bingham model is deemed suitable for the present work, it will be most likely suitable also for turbulent flows, provided that the rheological analysis is carried out with an appropriate shear rate range (Singh et al., 2016). In the context of a ship moving through mud, the shear rate can range from zero in undisturbed fluid regions to $\sim 10^4\,\mathrm{s}^{-1}$ in the turbulent boundary layer. How to reliably characterise the rheology of mud in such a wide range of shear rates remains, however, an open question.

Lastly, since a ship moving above (i.e. not through) a mud layer can still experience a significant increase of resistance due to the mud–water undulation, it would be worthwhile to investigate the accuracy of the Bingham model also for these types of scenarios.

CRediT authorship contribution statement

S. Lovato: Writing –original draft, Writing – review & editing, Conceptualization, Methodology, Software, Data curation, Validation, Formal analysis, Investigation, Visualization, Supervision. **A. Kirichek:** Writing – review & editing, Conceptualization, Resources, Supervision, Project administration, Funding acquisition. **S.L. Toxopeus:** Writing – review & editing, Resources, Formal analysis, Supervision. **J.W. Settels:** Writing – review & editing, Formal analysis, Supervision. **G.H. Keetels:** Writing – review & editing, Supervision, Funding acquisition.

Declaration of competing interest

The authors declare that they have no known competing financial interests or personal relationships that could have appeared to influence the work reported in this paper.

Acknowledgements

This research is funded by the Division for Earth and Life Sciences (ALW) with financial aid from the Netherlands Organization for Scientific Research (NWO) with Grant No. ALWTW.2016.029. The experimental part of the research is funded by Topconsortium voor Kennis en Innovatie (TKI) Deltatechnologie, Port of Rotterdam and Hamburg Port Authority. Calculations were performed on the Marclus4 (MARIN) cluster. The research support from MARIN is partly funded by the Dutch Ministry of Economic Affairs. This study was carried out within the framework of the MUDNET academic network: https://www.tudelft.nl/mudnet/. The authors wish to thank Lynyrd de Wit, Arno Talmon, Marcel Busink, Floris van Rees, Pavan Goda and Ahmad Shakeel for their help with the experimental part.

References

Deltares, Water and Soil Flume, https://www.deltares.nl/en/facilities/water-soil-flume.

ASME PTC Committee, 2009. Standard for Verification and Validation in Computational Fluid Dynamics and Heat Transfer: ASME V&V 20. The American Society of Mechanical Engineers (ASME), (ISSN: 01604120).

Barth, R., van der Made, C., Bourgonjen, L., van Dijken, J., Vantorre, M., Verwilligen, J., 2016. Manoeuvring with negative underkeel clearance: 2nd full scale field test in the port of Delfzijl. In: 4Nd MASHCON-International Conference on Ship Manoeuvring in Shallow and Confined Water with Special Focus on Ship Bottom Interaction. pp. 262–271.

Brouwer, J., Tukker, J., Klinkenberg, Y., van Rijsbergen, M., 2019. Random uncertainty of statistical moments in testing: Mean. Ocean Eng. 182, 563–576. http://dx.doi.org/10.1016/j.oceaneng.2019.04.068.

Chan, I.-C., Liu, P.L.-F., 2009. Responses of Bingham-plastic muddy seabed to a surface solitary wave. J. Fluid Mech. 618, 155–180. http://dx.doi.org/10.1017/S0022112008004357.

Chhabra, R.P., Richardson, J.F., 2008. Non-Newtonian Flow and Applied Rheology. Elsevier, p. 536. http://dx.doi.org/10.1016/B978-0-7506-8532-0.X0001-7.

Coussot, P., Piau, J.M., 1994. On the behavior of fine mud suspensions. Rheol. Acta 33 (3), 175–184. http://dx.doi.org/10.1007/BF00437302.

Delefortrie, G., Vantorre, M., Eloot, K., 2005. Modelling navigation in muddy areas through captive model tests. J. Mar. Sci. Technol. 10 (4), 188–202. http://dx.doi.org/10.1007/s00773-005-0210-5.

Dzuy, N.Q., Boger, D.V., 1985. Direct yield stress measurement with the vane method. J. Rheol. 29 (3), 335–347. http://dx.doi.org/10.1122/1.549794.

Eça, L., Hoekstra, M., 2009. Evaluation of numerical error estimation based on grid refinement studies with the method of the manufactured solutions. Comput. & Fluids 38 (8), 1580–1591. http://dx.doi.org/10.1016/j.compfluid.2009.01.003.

Eça, L., Hoekstra, M., 2014. A procedure for the estimation of the numerical uncertainty of CFD calculations based on grid refinement studies. J. Comput. Phys. 262, 104–130. http://dx.doi.org/10.1016/j.jcp.2014.01.006.

Ellwood, K.R.J., Georgiou, G.C., Papanastasiou, T.C., Wilkes, J.O., 1990. Laminar jets of Bingham-plastic liquids. J. Rheol. 34 (6), 787–812. http://dx.doi.org/10.1122/1.550144.

Ferziger, J.H., Perić, M., 1996. Computational Methods for Fluid Dynamics. Springer Berlin Heidelberg, Berlin, Heidelberg, http://dx.doi.org/10.1007/978-3-642-97651-3.

Frigaard, I.A., Nouar, C., 2005. On the usage of viscosity regularisation methods for visco-plastic fluid flow computation. J. Non-Newton. Fluid Mech. 127 (1), 1–26. http://dx.doi.org/10.1016/j.jnnfm.2005.01.003.

Gao, Z., Yang, H., Xie, M., 2015. Computation of flow around wigley hull in shallow water with muddy seabed. J. Coast. Res. 73, 490–495. http://dx.doi.org/10.2112/SI73-086.1.

Hirt, C., Nichols, B., 1981. Volume of fluid (VOF) method for the dynamics of free boundaries. J. Comput. Phys. 39 (1), 201–225. http://dx.doi.org/10.1016/0021-9991(81)90145-5.

International Organization for Standardization (ISO), 1995. Guide to the expression of uncertainty in measurement.

Jiang, F., Mehta, A.J., 1992. Some observations on fluid mud response to water waves. In: Dynamics and Exchanges in Estuaries and the Coastal Zone. pp. 351–376, URL https://agupubs.onlinelibrary.wiley.com/doi/abs/10.1029/CE040p0351.

Kaidi, S., Lefrançois, E., Smaoui, H., 2020. Numerical modelling of the muddy layer effect on Ship's resistance and squat. Ocean Eng. 199, 106939. http://dx.doi.org/10.1016/j.oceaneng.2020.106939.

Kirichek, A., Chassagne, C., Winterwerp, H., Vellinga, T., 2018. How navigable are fluid mud layers. Terra Et Aqua 151 (Summer), 6–18.

Klaij, C.M., Hoekstra, M., Vaz, G., 2018. Design, analysis and verification of a volume-of-fluid model with interface-capturing scheme. Comput. & Fluids 170, 324–340. http://dx.doi.org/10.1016/j.compfluid.2018.05.016.

Klaij, C.M., Vuik, C., 2013. SIMPLE-Type preconditioners for cell-centered, colocated finite volume discretization of incompressible Reynolds-averaged Navier-Stokes equations. Internat. J. Numer. Methods Fluids 71 (7), 830–849. http://dx.doi.org/10.1002/fld.3686.

Knoch, D., Malcherek, A., 2011. A numerical model for simulation of fluid mud with different rheological behaviors. Ocean Dyn. 61 (2–3), 245–256. http://dx.doi.org/10.1007/s10236-010-0327-x.

Ko-Fei, L., Mei, C.C., 1993. Long waves in shallow water over a layer of Bingham-plastic fluid-mud—I. Physical aspects. Internat. J. Engrg. Sci. 31 (1), 125–144. http://dx.doi.org/10.1016/0020-7225(93)90070-B.

Larsson, L., Raven, H.C., 2010. Ship Resistance and Flow. In: The Principles of Naval Architecture Series, ISBN: 978-0-939773-76-3.

Lemaire, S., Klapwijk, M., 2021. pyTST. Zenodo, 10.5281/zenodo.4428158.

Liu, K., Mei, C.C., 1989. Effects of wave-induced friction on a muddy seabed modelled as a Bingham-plastic fluid. J. Coast. Res. (ISSN: 07490208) 5 (4), 777–789.

Lovato, S., Keetels, G.H., Toxopeus, S.L., Settels, J.W., 2022. An eddy-viscosity model for turbulent flows of Herschel–Bulkley fluids. J. Non-Newton. Fluid Mech. 301, 104729. http://dx.doi.org/10.1016/j.jnnfm.2021.104729.

Lovato, S., Toxopeus, S.L., Settels, J.W., Keetels, G.H., Vaz, G., 2021. Code verification of non-Newtonian fluid solvers for single- and two-phase laminar flows. J. Verif. Valid. Uncertain. Quant. 6 (2), http://dx.doi.org/10.1115/1.4050131.

Lovato, S., Vaz, G., Toxopeus, S.L., Keetels, G.H., Settels, J.W., 2018. Code verification exercise for 2D Poiseuille flow with non-Newtonian fluid. In: Numerical Towing Tank Symposium. NuTTS, (October).

McBride, M., Boll, M., Briggs, M., et al., 2014. Harbour Approach Channels—Design Guidelines. PIANC Report No. 121, World Association for Waterborne Transport Infrastructure Brussels, Belgium.

Mei, C.C., Liu, K.-F., 1987. A Bingham-plastic model for a muddy seabed under long waves. J. Geophys. Res. 92 (C13), 14581. http://dx.doi.org/10.1029/JC092iC13p14581.

Mezger, T., 2020. The Rheology Handbook. Vincentz Network, http://dx.doi.org/10.1515/9783748603702.

Miloh, T., Tulin, M.P., Zilman, G., 1993. Dead-water effects of a ship moving in stratified seas. J. Offshore Mech. Arct. Eng. 115 (2), 105–110. http://dx.doi.org/10.1115/1.2920098.

Moore, F., 1959. The rheology of ceramic slip and bodies. Trans. Brit. Ceram. Soc. 58, 470–492.

Nirmalkar, N., Chhabra, R., Poole, R., 2013. Laminar forced convection heat transfer from a heated square cylinder in a Bingham plastic fluid. Int. J. Heat Mass Transfer 56 (1–2), 625–639. http://dx.doi.org/10.1016/j.ijheatmasstransfer.2012.08.049.

Papanastasiou, T.C., 1987. Flows of materials with yield. J. Rheol. 31 (5), 385–404. http://dx.doi.org/10.1122/1.549926.

Rudman, M., Blackburn, H., 2006. Direct numerical simulation of turbulent non-Newtonian flow using a spectral element method. Appl. Math. Model. 30 (11), 1229–1248. http://dx.doi.org/10.1016/j.apm.2006.03.005.

Sano, M., Kunitake, Y., 2018. Numerical solution for a ship-wave problem in a two-layer fluid using a double-model linearised interface condition. Ships Offshore Struct. 13 (3), 293–302. http://dx.doi.org/10.1080/17445302.2017.1371391.

Sellmeijer, R., van Oortmerssen, G., 1984. The effect of mud on tanker manoeuvres. Royal Inst. Nav. Archit. Trans. 126.

Shakeel, A., Kirichek, A., Chassagne, C., 2020a. Effect of pre-shearing on the steady and dynamic rheological properties of mud sediments. Mar. Pet. Geol. 116, 104338. http://dx.doi.org/10.1016/j.marpetgeo.2020.104338.

Shakeel, A., Kirichek, A., Chassagne, C., 2020b. Rheological analysis of mud from port of hamburg, Germany. J. Soils Sediments 20 (6), 2553–2562. http://dx.doi.org/10.1007/s11368-019-02448-7.

Shakeel, A., Kirichek, A., Chassagne, C., 2020c. Rheological analysis of natural and diluted mud suspensions. J. Non-Newton. Fluid Mech. 286, 104434. http://dx.doi.org/10.1016/j.jnnfm.2020.104434.

Shakeel, A., Kirichek, A., Talmon, A., Chassagne, C., 2021. Rheological analysis and rheological modelling of mud sediments: What is the best protocol for maintenance of ports and waterways? Estuar. Coast. Shelf Sci. 257, 107407. http://dx.doi.org/10.1016/j.ecss.2021.107407.

Singh, J., Rudman, M., Blackburn, H., 2017. The effect of yield stress on pipe flow turbulence for generalised Newtonian fluids. J. Non-Newton. Fluid Mech. 249, 53–62. http://dx.doi.org/10.1016/j.jnnfm.2017.09.007.

Singh, J., Rudman, M., Blackburn, H.M., Chryss, A., Pullum, L., Graham, L.J., 2016. The importance of rheology characterization in predicting turbulent pipe flow of generalized Newtonian fluids. J. Non-Newton. Fluid Mech. 232, 11–21. http://dx.doi.org/10.1016/j.jnnfm.2016.03.013.

Toorman, E.A., 1997. Modelling the thixotropic behaviour of dense cohesive sediment suspensions. Rheol. Acta 36 (1), 56–65. http://dx.doi.org/10.1007/BF00366724.

van Kessel, T., Blom, C., 1998. Rheology of cohesive sediments: comparison between a natural and an artificial mud. J. Hydraul. Res. 36 (4), 591–612. http://dx.doi.org/10.1080/00221689809498611.

van Leer, B., 1979. Towards the ultimate conservative difference scheme. V. A second-order sequel to Godunov's method. J. Comput. Phys. 32 (1), 101–136. http://dx.doi.org/10.1016/0021-9991(79)90145-1.

Vaz, G., Jaouen, F., Hoekstra, M., 2009. Free-surface viscous flow computations: Validation of URANS code FRESCO. In: Proceedings of OMAE2009, Honolulu, Hawaii, USA. pp. 425–437. http://dx.doi.org/10.1115/OMAE2009-79398.

Winterwerp, J., de Graaff, R., Groeneweg, J., Luijendijk, A., 2007. Modelling of wave damping at Guyana mud coast. Coast. Eng. 54 (3), 249–261. http://dx.doi.org/10.1016/j.coastaleng.2006.08.012.

Worrall, W., Tuliani, S., 1964. Viscosity changes during the ageing of clay-water suspensions. Trans. Brit. Ceram. Soc. 63, 167–185.

Wright, V., Krone, R., 1989. Aggregate structure in hyperconcentrated mud flows. J. Coast. Res. 117–125.

Wurpts, R.W., 2005. 15 Years experience with fluid mud: Definition of the nautical bottom with rheological parameters. Terra Et Aqua (ISSN: 03766411).

Zilman, G., Miloh, T., 1995. Hydrodynamics of a body moving over a mud layer - Part I: wave resistance. J. Ship Res. (ISSN: 00224502) 39 (3).